Efficient Prediction of Superlattice and Anomalous Miniband Topology from Quantum Geometry

Valentin Crépel[1] and Jennifer Cano[2,1]

[1]*Center for Computational Quantum Physics, Flatiron Institute, New York, New York 10010, USA*
[2]*Department of Physics and Astronomy, Stony Brook University, Stony Brook, New York 11794, USA*

Two-dimensional materials subject to long-wavelength modulations have emerged as novel platforms to study topological and correlated quantum phases. In this article, we develop a versatile and computationally inexpensive method to predict the topological properties of materials subjected to a superlattice potential by combining degenerate perturbation theory with the method of symmetry indicators. In the absence of electronic interactions, our analysis provides a systematic rule to find the Chern number of the superlattice-induced miniband starting from the harmonics of the applied potential and a few material-specific coefficients. Our method also applies to anomalous (interaction-generated) bands, for which we derive an efficient algorithm to determine all Chern numbers compatible with a self-consistent solution to the Hartree-Fock equations. Our approach gives a microscopic understanding of the quantum anomalous Hall insulators recently observed in rhombohedral graphene multilayers.

Subject Areas: Condensed Matter Physics, Topological Insulators

I. INTRODUCTION

The advent of moiré and, more generally, superlattice materials has ushered in a new era in condensed matter physics, providing fertile ground for the exploration and design of exotic quantum phases [1–4]. These systems, characterized by periodic modulations on the tens of nanometer scale, exhibit rich and tunable electronic properties due to the interplay between the low-energy physics of their constituents and the geometric properties of the long-wavelength modulation. Reverse engineering this rich phenomenology to identify the optimal combination of materials and long-wavelength modulation to observe a specific phase of interest has, however, proven to be a very challenging task. Indeed, understanding the phase diagram of a particular material platform has traditionally relied on the computation of the full superlattice band structure—a process often computationally intense and analytically opaque [5–10]—which is then used to derive effective models [11–16] that are finally studied using (costly) state-of-the-art numerical methods.

In this work, we propose an approximate but quick and versatile method for determining the topological phase diagram of superlattice materials using a few material-specific coefficients, circumventing the need for exhaustive band structure computations. More precisely, we rely on degenerate perturbation theory to analytically compute eigenvalues of crystalline rotation symmetry operators acting on the superlattice-induced minibands' eigenvectors at high-symmetry points of the reduced Brillouin zone determined by the superlattice potential. Our perturbative result requires only the knowledge of the superlattice geometry and a small number of form factors from the original material. The Chern number of the minibands can be extracted from these eigenvalues using the symmetry indicators from Ref. [17]. This analytic topological criterion is correct as long as the gaps opened at high-symmetry points for perturbative values of the superlattice amplitude do not close as the latter is tuned to its microscopically realistic value. While we primarily focus on superlattice materials, which are elegantly captured by a single topological phase diagram for each symmetry class (Table I), the perturbative method that we introduce is highly versatile: We successfully apply it to continuum models for twisted transition metal dichalcogenides and twisted bilayer graphene in Appendix C.

We then include interaction-induced (Hartree-Fock) corrections to the superlattice potential. In this context, the remarkable simplification offered by our perturbative symmetry-indicator framework is that the self-consistent Hartree-Fock theory is reduced to a small number of equations—one for each high-symmetry point—involving the symmetry eigenvalues of the miniband eigenvectors.

TABLE I.   Topology of the lowest superlattice-induced miniband determined by degenerate perturbation theory using symmetry indicators, in the absence of interactions. The first row specifies the C_n-rotational symmetry of the superlattice; $n = 2, 3, 4,$ or 6. The second row indicates the high-symmetry points of the reduced Brillouin zone (rBZ) fixed by the superlattice and the harmonics of the potential (third row) that resonantly couple these high-symmetry points to their degenerate rotated images. Row four gives the Chern number $C_n = C(\mathrm{mod}\,n)$ of the lowest superlattice-induced miniband in the long-period limit, where the rBZ is small compared to the scale on which the quantum geometry of the original material varies. In this limit, the Chern number depends on only a finite set of superlattice harmonics (real for even n; see row three) and on the Berry flux ϕ_B of the original material enclosed in the rBZ. Here, $\lfloor x \rfloor$ denotes the floor function, Θ the Heaviside function, and θ the phase of the only relevant complex harmonic (when $n = 3$). Away from this limit, C_n can still be analytically determined within our framework by replacing the Berry flux ϕ_B by a small number of material-specific form factors M_q, which are gathered in row five; U_p denotes the matrix representation of the $2\pi/p$ rotation, which acts on a Bloch eigenvector $|q\rangle$ with quasimomentum q. Combining the form factors (fifth row) with the potential harmonics (third row) yields loop phases $\Phi_q^{\circlearrowleft}$, which determine the general topological phase diagram in the last row. The same colors are used across the entire row for identical values of C_n.
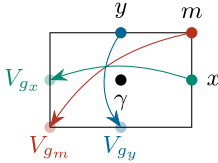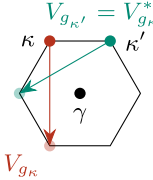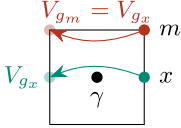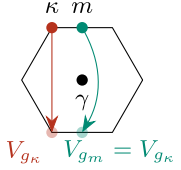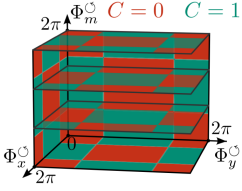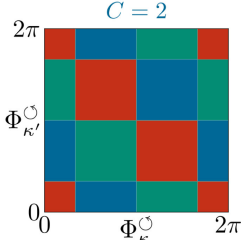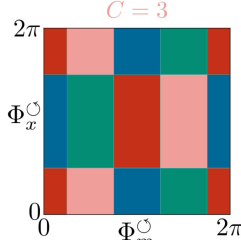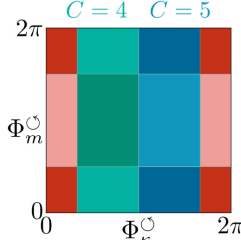
Symmetry group C_n	$n = 2$	$n = 3$	$n = 4$	$n = 6$
Reduced BZ				
Resonant harmonics determining C_n in the long-period limit	$V_{g_x}, V_{g_y}, V_{g_m} \in \mathbb{R}$	$V_{g_\kappa} = |V|e^{i\theta} \in \mathbb{C}$	$V_{g_x} \in \mathbb{R}$	$V_{g_\kappa} \in \mathbb{R}$
Chern number C_n in the long-period limit	$\Theta(-V_{g_x} V_{g_y} V_{g_m})$	$\sum_{\epsilon=\pm 1} \left\lfloor \frac{2\pi + 6\epsilon\theta - \phi_B}{4\pi} \right\rfloor$	$\left\lfloor \frac{\pi - \phi_B}{2\pi} \right\rfloor$	$1 - v + 2\left\lfloor \frac{2\pi v - \phi_B}{4\pi} \right\rfloor$ with $v = \Theta(V_{g_\kappa})$
Form factors for the general case	$M_q = \langle q|U_2|q\rangle$ $q \in \{\gamma, x, y, m\}$	$M_q = \langle q|U_3|q\rangle$ $q \in \{\gamma, \kappa, \kappa'\}$	$M_\gamma = \langle \gamma|U_4|\gamma\rangle$ $M_m = \langle m|U_4|m\rangle$ $M_x = \langle x|U_4^2|x\rangle$	$M_\gamma = \langle \gamma|U_6|\gamma\rangle$ $M_m = \langle m|U_6^3|m\rangle$ $M_\kappa = \langle \kappa|U_6^2|\kappa\rangle$
Chern number C_n in the general case as a function of the loop phases $\Phi_q^{\circlearrowleft} =$ $p(q) \arg \frac{V_{g_q} M_q^*}{M_\gamma^*}$				

TABLE II.   Efficient determination of all Chern numbers $C_n = C(\mathrm{mod}\,n)$ compatible with a self-consistent Hartree-Fock solution on a rBZ set by an interaction-generated superlattice potential using degenerate perturbation theory. For convenience, we repeat here the definitions given in the main text: n encodes the discrete rotational symmetry C_n of the problem in the presence of the superlattice, $q_{0,1,2}$ run over the high-symmetry points of the rBZ and their rotated images excluding the rBZ center γ, and $p(q)$ denotes the largest divisor of n such that q is left invariant by a $2\pi/p$ rotation around γ up to reciprocal lattice vectors of the superlattice. The evaluation of each $\Gamma_{q_0}^{(n)}$ requires a handful of elementary operations that involve only the Chern number C_n, the form factors Λ_{q_2,q_1}, and the Fourier transform of the two-body interaction potential $v(q)$ [see Eq. (B2)].

1. Compute a finite number of form factors $\Lambda_{q_2,q_1} = \langle \chi(q_2)|\chi(q_1)\rangle$ (12 at most).
2. For all possible C_n between 0 and $(n - 1)$:
3. Evaluate the $\Gamma_{q_0}^{(n)}[C_n, v, \Lambda]$ (given explicitly in Appendix B) for all high-symmetry points q_0 depicted in Table I.
4. If $|\arg[-\Gamma_{q_0}^{(n)}]| < \pi/p(q_0)$ for all q_0 [Eq. (27)]:
5. C_n is compatible with a self-consistent Hartree-Fock solution within degenerate perturbation theory.

To solve these equations, it is sufficient to loop over the finite different values that they can take and, for each set of such eigenvalues, perform a simple self-consistency check involving a small number of the material's form factors. This provides an efficient topological criterion that not only circumvents the computation of the superlattice band structure, but also eliminates the need for an effective model to describe the band structure and a full-fledged Hartree-Fock equation for the effective model.

Our approach enables a streamlined and efficient characterization of the topological properties of complex superlattice heterostructures. Our work applies to superlattices that are externally imposed by gate nanopatterning [3,18–28] or a moiré potential arising from proximity coupling to another layer or a substrate with a nearly matched lattice constant and no low-energy degrees of freedom [29–37], as well as to "anomalous" superlattices spontaneously generated by electronic interactions [36,38–45]. While similar ideas have been used before on a case-by-case basis, e.g., Refs. [46–50], the present work gives a systematic list of inputs to determine the Chern number analytically (see Tables I and II). These results can be efficiently applied to new moiré systems as they arise. We illustrate the predictive power of our method by analyzing biased rhombohedral graphene multilayers in the presence of a nearly aligned h-BN substrate, for which we nail down a remarkable coincidence of length scales responsible for the emergence of the quantum anomalous Hall behaviors observed in penta- and hexalayer stacks [36,38].

II. SUMMARY OF RESULTS

For clarity of presentation, let us briefly summarize the main results obtained in this manuscript and indicate where they are derived. Our starting point is a two-dimensional material or heterostructure, which, upon weak doping, features isolated Fermi pockets centered around some high-symmetry points γ_v of its Brillouin zone, with v a valley index labeling the different pockets. Our goal is to predict the topological invariant of the minibands emerging around γ_v when a superlattice potential $V(r)$ with discrete rotation symmetry is applied to the sample and/or self-consistently generated by interactions. As previously mentioned, this is achieved by combining degenerate perturbation theory with the method of symmetry indicators. We treat the valley v as a good quantum number, which implicitly requires the superlattice to vary slowly on the atomic scale to avoid scattering between the different pockets, and also assume that a single electronic band is relevant near each γ_v.

We start in Sec. III with the case of an externally applied superlattice potential that identically couples to all internal degrees of the material or heterostructure under consideration. The results of our perturbative analysis in this situation are summarized in Table I, which we quickly describe. First, the minimal set of parameters necessary to solve the degenerate-perturbation theory at the high-symmetry points of the rBZ set by the superlattice is identified for all possible rotation symmetry groups $\mathcal{C}_n$ of the system around each valley γ (first two rows in Table I). These parameters come in two varieties: harmonics of the superlattice potential, that resonantly couple states whose degeneracy is imposed by $\mathcal{C}_n$ symmetry, and material-specific form factors between these degenerate states (third and fifth row in Table I, respectively). The parameters are combined into gauge-invariant quantities, coined loop phases for reasons detailed in Sec. III B, from which the Chern number modulo n, C_n, of the lowest band can be derived analytically using the method of symmetry indicators [17] (summarized in Sec. III A). The result of this calculation for each symmetry group, described in Sec. III C, is presented in the last row in Table I. In the limit where the period of the superlattice is long, we can replace the contribution of form factors in the loop phases by a function of ϕ_B, the Berry flux of the original material enclosed by the rBZ. This simplifies the analytical formula for C_n, derived in Sec. III C and given in the fourth row in Table I.

These results can be straightforwardly extended to potentials which couple nontrivially to the microscopic degrees of freedom according to a spatially uniform matrix P with the mere replacement $M_q = \langle q|U_{p(q)}|q\rangle \to \langle q|PU_{p(q)}|q\rangle$ in the fifth row in Table I, with $p(q)$ the largest divisor of n such that q is left invariant by a $2\pi/p$ rotation around γ up to reciprocal lattice vectors of the superlattice, $|q\rangle$ the material's Bloch vectors at momentum $\gamma + q$, and U_p the representation of the $(2\pi/p)$ rotation with the same dimension as $|q\rangle$. Naturally, the explicit form of P depends on the physical situation considered. For concreteness, we demonstrate how this construction works in Sec. V B for the case of a graphene multilayer stack in which the bottom layer is in contact with a nearly aligned h-BN substrate. In that case, P represents the projector onto the atoms closest to the substrate. Similarly, we can include the perturbative effect of interlayer tunneling in moiré homobilayers using a modified version of the P projector, as described in Appendix C.

In Sec. IV, we consider Hartree-Fock corrections to the superlattice potential generated by interactions. Under a so-called "resonant" approximation explained in Sec. IV A, these corrections can be computed from the sole knowledge of the form factors between all high-symmetry points of the rBZ and the symmetry eigenvalues at these high-symmetry points. This allows us to derive self-consistent equations for the symmetry eigenvalues that depend on only a few material-specific form factors and the harmonics of the externally applied superlattice potential. Within our formalism, the self-consistent nature of these equation adds only a minimal computational cost to the determination of the Chern number. Indeed, the symmetry eigenvalues can take only a finite number of values, over which we can loop to compute the Hartree-Fock corrections and check whether

they give rise to self-consistent solutions for the symmetry eigenvalues at all high-symmetry points. When interactions effects dominate the physics of the system under consideration, i.e., if the amplitude of the superlattice is negligible, this loop over symmetry eigenvalues simplifies to a loop over the n possible Chern numbers (modulo n), as shown in Sec. IV B and sketched as an algorithm in Table II. This algorithm necessitates only the evaluation of auxiliary parameters [the $\Gamma_{q_0}^{(n)}$ defined in Eq. (B2)] that depend on a finite set of material form factors and on the two-body interaction potential.

Finally, in Sec. V, we apply our formalism to biased rhombohedral graphene multilayers stacked above a nearly aligned h-BN substrate, in which quantum anomalous Hall behaviors have recently been experimentally observed [36,38]. Not only does our perturbative topological criterion correctly capture the phases observed experimentally, but it also offers a unique analytical insight into the remarkable coincidence responsible for the observed quantum anomalous Hall behaviors. More precisely, a careful inspection of the algorithm in Table II shows the transition to a quantum anomalous Hall phase with Chern number $C_3 = -1 \pmod 3$ when the phase of the Fock term reaches a value $> \pi/3$. This phase depends on only the form factors of the graphene stack and is directly proportional to the flux of Berry curvature threading the rBZ. Computing this flux, we find that the transition to a topological insulating state occurs when the superlattice period $a_{\text{super}}^* \simeq (v_F K a_0/0.6t_1) = 11$ nm, where v_F, K, and a_0, respectively, denote the Fermi velocity, Brillouin zone corner, and lattice constant of the graphene multilayer, while t_1 represents the nearest-neighbor interlayer tunneling amplitude within the stack. The exceptional coincidence explaining the experimental observation of quantum anomalous Hall behaviors in Refs. [36,38] is that, for a graphene/h-BN twist of about 1°, the superlattice potential imposed by the h-BN substrate lies very close to this special value a_{super}^*.

III. NONINTERACTING THEORY

In this section, we introduce our methodology for determining the Chern number of the lowest-energy band in the rBZ resulting from an externally applied superlattice potential $V(r)$, discarding the effects of interactions that are included in Sec. IV.

A. Method

Let us focus on a single valley γ and describe the method of symmetry indicators for determining the topological content of the superlattice-induced minibands. To do this, we first introduce some notations. We, respectively, call ε_q and $|\chi(q)\rangle$ the energy and the periodic part of the Bloch eigenvector at momentum $k = \gamma + q$ of the band giving rise to the Fermi pocket at γ. We decompose the superlattice potential into Fourier components

$$V(r) = -\sum_g V_g e^{ig \cdot r}, \qquad (1)$$

where $V_{-g} = V_g^*$ is required for the potential to be real, while the overall negative sign is conventional and chosen to recall that electrons have negative electric charge. The quasimomentum k in the original band spans the full Brillouin zone (BZ) of the original material, which is folded due to the superlattice potential into a rBZ defined by the g vectors. We denote by $\mathcal{C}_n$ the largest subgroup of the point symmetry group at γ under which the potential $V(r)$ is invariant. Under R_n, the rotation by $2\pi/n$, it follows that $\varepsilon_{R_n q} = \varepsilon_q$ and $V_{R_n g} = V_g$. We choose a gauge in which the action of R_n on the Bloch wave vectors is given by a representation U_n which satisfies

$$U_n|\chi(q)\rangle = \lambda_n(\gamma)|\chi(R_n q)\rangle, \qquad \lambda_n(\gamma) = e^{(2i\pi/n)\nu_n(\gamma)}, \quad (2)$$

for all q in the rBZ, where $\lambda_n(\gamma)$ is the R_n eigenvalue of $|\chi(0)\rangle$. We take $\nu_n(\gamma)$ to be an integer, which is valid in the absence of spin-orbit coupling.

With these definitions, the Hamiltonian at momentum $k = \gamma + q$ projected in the band of interest takes the form

$$H(q) = \sum_g \varepsilon_{q+g} c_{q+g}^\dagger c_{q+g} - V_g \Lambda_{q+g,q} c_{q+g}^\dagger c_q, \quad (3)$$

where c_q is the fermionic annihilation operator corresponding to $|\chi(q)\rangle$, the form factor $\Lambda_{q',q} = \langle\chi(q')|\chi(q)\rangle$ arises from projecting onto a single band, and q runs over the BZ. The gauge chosen above makes clear that these form factors, and, hence, $H(q)$, are $\mathcal{C}_n$ symmetric.

To determine whether the lowest-energy miniband of Eq. (3) has nontrivial topology, we rely on the symmetry indicators developed in Ref. [17]. There, it is proved that the Chern number C of an isolated band with R_n symmetry can be determined modulo n by the product of $\lambda_p(q_p)$, the R_p eigenvalues of the band's Bloch eigenvectors at momenta q_p of the rBZ invariant under R_p, where p runs over all divisors of n. Because $n = 2, 3, 4, 6$ can take only four values in two dimensions, this result can be written explicitly as

$$e^{(2i\pi/2)C_2} = \lambda_2(\gamma)\lambda_2(m)\lambda_2(x)\lambda_2(y) \quad \text{for } n = 2,$$
$$e^{(2i\pi/3)C_3} = \lambda_3(\gamma)\lambda_3(\kappa)\lambda_3(\kappa) \quad \text{for } n = 3,$$
$$e^{(2i\pi/4)C_4} = \lambda_4(\gamma)\lambda_4(m)\lambda_2(x) \quad \text{for } n = 4,$$
$$e^{(2i\pi/6)C_6} = \lambda_6(\gamma)\lambda_3(\kappa)\lambda_2(m) \quad \text{for } n = 6, \qquad (4)$$

with $C_n = C(\mathrm{mod} n)$, and where the definition of the high-symmetry points is given graphically in the second line in Table I for all n. We discard the spin contribution, which does not play any role in the absence of spin-orbit coupling.

In the rest of this section, we determine whether the lowest superlattice-induced miniband from the γ valley is topological using the symmetry indicator formulas [Eq. (4)] by analytical solution of the band-projected superlattice Hamiltonian [Eq. (3)] at the high-symmetry points depicted in the second line in Table I, which is possible when $V(r)$ is treated as a perturbation. The topological invariants obtained by this degenerate perturbation theory remain valid for nonperturbative amplitudes of the superlattice potential as long as the gaps opened for small $V(r)$ do not close when the amplitude of the superlattice is increased to its full value.

B. A single high-symmetry point

We now compute the eigenvalues appearing in Eq. (4) for the lowest-energy band formed by the superlattice at all the high-symmetry points depicted in the second line in Table I. As explained above, we compute these eigenvalues assuming a weak superlattice potential, which enables an analytical solution of Eq. (3) using degenerate perturbation theory. The obtained eigenvalues remain unchanged for nonperturbative amplitudes of the superlattice potential as long as the gaps opened for small $V(r)$ do not close as $V(r)$ is increased to its full value. The results obtained here are used in Sec. III C to predict which combinations of superlattice geometry and form factors yield topological minibands.

Let us consider a high-symmetry point $q_0 \neq \gamma$ in the rBZ with point group symmetry $\mathcal{C}_p$, where p necessarily divides n. We discard γ from the present discussion, since its $\mathcal{C}_n$ eigenvalue $\lambda_n(\gamma)$ is a property of the material under consideration that does not change under a weak superlattice potential. Discarding γ restricts $p \in \{2, 3, 4\}$ to only three distinct values [see Eq. (4)]. The diagonalization of $H(q_0)$ for weak superlattice potential can be obtained by projecting the Hamiltonian into the subspace of degenerate eigenvectors with momenta q related by $\mathcal{C}_p$ symmetry to q_0, i.e., in the basis $[|\chi(q)\rangle, q \in \mathcal{B}(q_0)]$ with

$$\mathcal{B}(q_0) = \{q_k = R_n^{kn/p} q_0 = R_p^k q_0 | k = 0, \ldots, p-1\}. \quad (5)$$

The Hamiltonian projected onto the degenerate subspace $\mathcal{B}(q_0)$ takes the circulant form

$$PH(q_0)P = \begin{bmatrix} a_0 & a_{p-1} & \cdots & a_2 & a_1 \\ a_1 & a_0 & a_{p-1} & & a_2 \\ \vdots & a_1 & a_0 & \ddots & \vdots \\ a_{p-2} & & \ddots & \ddots & a_{p-1} \\ a_{p-1} & a_{p-2} & \cdots & a_1 & a_0 \end{bmatrix}, \quad (6)$$

with P the projector onto the basis of Eq. (5), and where

$$a_0 = \varepsilon_{q_0}, \qquad a_{k>0} = -V_{q_k - q_0} \Lambda_{q_k, q_0} = a_{p-k}^*. \quad (7)$$

The eigenvalues and eigenvectors of $PH(q_0)P$ are obtained by discrete Fourier transform and read

$$E_\nu = \sum_{k=0}^{p-1} \omega_p^{\nu k} a_k, \quad |\phi_\nu\rangle = \sum_{k=0}^{p-1} \frac{\omega_p^{-\nu k} |\chi(q_k)\rangle}{\sqrt{p}}, \quad \omega_p = e^{2i\pi/p}, \quad (8)$$

from which it is clear that $|\phi_\nu\rangle$ has $\mathcal{C}_p$ eigenvalue

$$\langle \phi_\nu | U_p | \phi_\nu \rangle = [\lambda_n(\gamma)]^{n/P} \omega_p^\nu, \qquad U_p = (U_n)^{n/p}. \quad (9)$$

The $\mathcal{C}_p$ eigenvalues in Eq. (9) belong to the p lowest-energy minibands at q_0 in the rBZ. To apply the symmetry indicator formula to the *lowest* miniband, we need the $\mathcal{C}_p$ eigenvalue of that specific band. Thus, we now determine the smallest E_ν. We first rewrite the energies in Eq. (8) using the relation $a_k = a_{p-k}^*$ to find

$$E_\nu = \varepsilon_{q_0} + \begin{cases} \mathrm{Re}[\omega_2^\nu a_1] & p = 2, \\ \mathrm{Re}[2\omega_3^\nu a_1] & p = 3, \\ \mathrm{Re}[2\omega_4^\nu a_1 + \omega_2^\nu a_2] & p = 4. \end{cases} \quad (10)$$

Under the assumption that the largest harmonics of the potential dominate over the second one when $p = 4$, i.e., when $a_2 = 0$, the energy E_ν is minimized for all p when the argument of $\omega_p^\nu a_1$ is closest to π modulo 2π. Using $\arg[\omega_p^\nu a_1] = \pi + \arg(V_{q_1-q_0} \Lambda_{q_1,q_0}) + 2\nu\pi/p$, the energy is minimized when the integer ν is closest to $[-p \arg(V_{q_1-q_0} \Lambda_{q_1,q_0})/2\pi]$ modulo p. This is realized for

$$\nu_p(q_0) = \left\lfloor \frac{\pi - \Phi_{q_0}^{\circlearrowleft}}{2\pi} \right\rceil, \qquad \Phi_{q_0}^{\circlearrowleft} = p \arg(V_{g_{q_0}} \Lambda_{q_1,q_0}), \quad (11)$$

where $\lfloor x \rceil$ denotes the largest integer smaller than x and $g_{q_0} = q_1 - q_0$. Let us highlight that the phase $\Phi_{q_0}^{\circlearrowleft}$ can also be written as
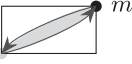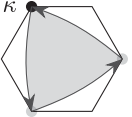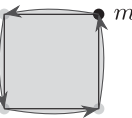
$$\Phi_{q_0}^{\circlearrowleft} = p \, \arg \left[V_{g_{q_0}} \frac{\langle \chi(q_0) | U_p^\dagger | \chi(q_0) \rangle}{\langle \chi(\gamma) | U_p^\dagger | \chi(\gamma) \rangle} \right], \quad (12)$$

which involves only expectation values of Bloch eigenvectors that are local in momentum space and can, therefore, be efficiently computed from results of a density functional theory or tight-binding calculation of the original material. This is the form of the loop phases given in Table I, where we use a different symbol:

$$M_{q_0} = \langle \chi(q_0) | U_p | \chi(q_0) \rangle, \quad (13)$$

for the form factors to make clear that the formula provided is independent of the gauge chosen for the Bloch vectors.

TABLE III. Geometric factor $r_p(q_0)$ measuring the fraction of the rBZ spanned by the $(q_k)_{k=0,...,p}$ loop for all high-symmetry points q_0 appearing in Eq. (4), where the point group symmetry at q_0 is $\mathcal{C}_p$. The last column shows a representative loop for each case considered, where the area enclosed by the loop is colored in red while the rBZ is shown with a solid black line. In the first two cases, this area should be understood to vanish as the loop contracts to a point or to a line.

p	q_0	$r_p(q_0)$	$(q_k)_{k=0,...,p}$ loop
2, 3, 4, 6	γ	0	
2	x, y, m	0	
3	κ, κ'	1/2	
4	m	1	

Only in the C_n-symmetric gauge chosen at the beginning of the section do we have $M_{q_0} = \Lambda_{q_0,q_1}$.

The phases $\Phi_{q_0}^{\circlearrowleft}$ have a simple physical interpretation: They correspond to the total phase acquired along the discrete loop $\{q_k = R_p^k q_0\}_{k=0,...,p}$ connecting degenerate high-symmetry points, including contributions from both the potential harmonics and the Berry flux enclosed within the loop (explaining the $\circlearrowleft$ superscript). To see this, use the $\mathcal{C}_p$ symmetry to rewrite

$$\Phi_{q_0}^{\circlearrowleft} = \arg\left[\prod_{k=0}^{p-1} V_{q_{k+1}-q_k}\Lambda_{q_{k+1},q_k}\right]. \quad (14)$$

This manifestly gauge-invariant form allows one to interpret $\Phi_{q_0}^{\circlearrowleft}$ as the phase acquired along the discrete loop connecting q_0 to its R_p-rotated images (see Table III for illustrations). In practice, Eq. (14) should also be used when the gauge chosen in a particular calculation is not $\mathcal{C}_p$ symmetric, as assumed when writing Eq. (17) [recall the discussion of gauge choice above Eq. (3)].

In the limit where the period of the superlattice is long—more precisely, when the primitive reciprocal lattice vectors of the rBZ are small compared to the typical scale on which the quantum geometry of the original band varies—the product of form factors in Eq. (14) gives the total Berry flux of the original material enclosed within the loop, and we can write

$$\Phi_{q_0}^{\circlearrowleft} \simeq p \arg[V_{g_{q_0}}] + r_p(q_0)\phi_B, \qquad \phi_B = \Omega_\gamma A_{\mathrm{rBZ}}, \quad (15)$$

with ϕ_B the total Berry flux enclosed by the rBZ, written as the product of Ω_γ, the Berry curvature at γ, with the rBZ area A_{rBZ}. The geometrical factor $r_p(q_0)$ denotes the fraction of the rBZ area enclosed by the $(q_k)_{k=0,...,p-1}$ loop. The values of this geometric factor for the different high-symmetry points are tabulated in Table III. When p is even, R_2 is a symmetry element, which implies $V_g = V_{R_2g=-g} = V_g^*$; i.e., V_g is real. Thus, we can substitute

$$\arg(V_g) = \frac{\pi}{2}[1 - \mathrm{sgn}(V_g)] = \pi\Theta(-V_g) \quad (16)$$

in the definition of $\Phi_p^{\circlearrowleft}(q_0)$, where $\mathrm{sgn}(x)$ and $\Theta(x)$, respectively, denote the sign and Heaviside functions.

Combining Eqs. (9) and (11), we finally obtain

$$\lambda_p(q_0) = e^{(2i\pi/p)[\nu_n(\gamma)+\nu_p(q_0)]}. \quad (17)$$

This is the first main result of this paper. It relates the symmetry eigenvalues $\lambda_p(q_0)$ of the lowest superlattice-induced miniband to the gauge-invariant loop phase $\Phi_{q_0}^{\circlearrowleft}$, which includes the effect of the potential and of the form factors of the material. These loop phases can be efficiently computed from the sole knowledge of the superlattice geometry, the Bloch states at high-symmetry points, and the matrix representation U_n of the $2\pi/n$ rotation R_n in their Hilbert space. In the long-period limit, the dependence on the form factors is entirely carried by ϕ_B, the total Berry flux of the original material threading the reduced Brillouin zone defined by the superlattice potential. Together, Eqs. (4) and (17) reduce the problem of computing the Chern number of the lowest superlattice-induced miniband to the calculation of a finite number of matrix elements, as we carry out in the next section.

C. Topological invariants

We now combine the expression for the Chern number in terms of symmetry eigenvalues with our perturbative calculation of the latter to determine conditions under which the lowest superlattice-induced miniband acquires a Chern number. Using Eq. (17), the Chern number modulo n in Eq. (4) formally becomes

$$C_n = \nu_n(\gamma) + \sum_{q_0\neq\gamma}\frac{n}{p(q_0)}[\nu_n(\gamma) + \nu_p(q_0)]$$

$$= \sum_{q_0\neq\gamma}\frac{n}{p(q_0)}\nu_p(q_0), \quad (18)$$

where q_0 runs over the high-symmetry points of the Brillouin zone excluding γ, $\nu_p(q_0)$ is given in Eq. (11), and $p(q_0)$ is the largest divisor of n for which $R_n^{n/p}q_0 = q_0$.

To obtain the second line in Eq. (18), we remove a multiple of $n\nu_n(\gamma)$ from the first line, since C_n is defined modulo n.

In Appendix A, we treat the different values of $n = 2, 3, 4, 6$ separately, identify the independent variables that determine C_n in each case, and simplify the formula for C_n in the long-period limit [discussed above Eq. (15)]. The results populate Table I, which provides a concise summary of our noninteracting results.

As an illustrative example applying our results, we now derive the recent observation, made in several recent works [3,28,44,51,52], that superlattices with honeycomb geometry have a stronger propensity to form topological minibands than triangular ones. To see this, let us focus on the $n = 3$ column in Table I and rely on the long-wavelength formula for the Chern number $C_3 = C$ (mod 3). We first consider a triangular superlattice ($\theta = 0$), which, in the absence of Berry curvature at γ in the original material ($\phi_\mathrm{B} = 0$), yields loop phases equal to zero for both κ and κ'. This corresponds to the origin of the $n = 3$ topological phase diagram in Table I (last row), where $C_3 = 0$. The addition of Berry curvature at γ moves both loop phases by the same amount, i.e., along the first diagonal of the topological phase diagram, such that the system remains in the $C_3 = 0$ phase even for nonzero values of ϕ_B. In fact, the long-wavelength analytic formula shows that reaching a state with nonzero Chern number requires the Berry flux through the rBZ to reach $|\phi_\mathrm{B}| > 2\pi$, which is highly unlikely for small rBZ. On the other hand, we observe that honeycomb superlattices ($\theta = \pi$) favor topological states for any infinitesimal amount of enclosed Berry curvature ϕ_B. This can be seen in the $n = 3$ topological phase diagram in Table I, where the honeycomb case with $\phi_\mathrm{B} = 0$ corresponds to the (π, π) point, which is surrounded along the first diagonal by phases with $C_3 \neq 0$. Adding Berry curvature necessarily drives the system into one of those topological phases. This can also be seen by plugging $\theta = \pi$ in the long-wavelength formula in Table I, yielding $C_3 = 1 + 2\lfloor -\phi_\mathrm{B}/4\pi \rfloor$ that is either equal to 1 ($\phi_\mathrm{B} < 0$) or to -1 ($\phi_\mathrm{B} > 0$) for $|\phi_\mathrm{B}| < 4\pi$.

IV. EFFECTS OF INTERACTIONS

The applicability of the results derived in Sec. III relies on two main assumptions. The first, explicitly stated in Sec. III A, is that the gaps opened by the superlattice potential at its full strength do not close as the potential strength is turned down to a perturbatively small value. The second, implicit in the single-particle formalism of the last section, is that interactions do not contribute to the gap opening at the high-symmetry points. In this section, we relax this second hypothesis and demonstrate that the Chern number of the lowest miniband can still be determined from a small number of form factors of the original band structure in the presence of interactions when the interactions are treated perturbatively. As in the previous sections, the results obtained in this perturbative limit

remain correct if the gaps at high-symmetry points of the rBZ do not close as the superlattice amplitude and interaction strength are tuned to their full values.

A. Self-consistent Hartree-Fock equations
1. Hartree-Fock potentials

We consider a positive two-body interaction potential $v(q) > 0$ with continuous rotation symmetry and project it onto the relevant band around γ to obtain, within the Hartree-Fock approximation, an updated form of the Hamiltonian in Eq. (3):

$$H(q) = \sum_g \varepsilon_{q+g} c^\dagger_{q+g} c_{q+g} + [V^\mathrm{HF}_{q,g} - V_g]\Lambda_{q+g,q} c^\dagger_{q+g} c_q, \quad (19)$$

where the interaction-induced part of the effective potential V^HF arises from nonzero expectation values $\rho_{k,g} = \Lambda_{k+g,k}\langle c^\dagger_{k+g} c_k \rangle$ in the ground state and reads

$$V^\mathrm{HF}_{q,g} = V^\mathrm{H}_g - V^\mathrm{F}_{q,g}, \qquad V^\mathrm{H}_g = \int \frac{\mathrm{d}^2 k}{A_\mathrm{BZ}} v(g)\rho^*_{k,g}, \quad (20\mathrm{a})$$

$$V^\mathrm{F}_{q,g} = \int' \frac{\mathrm{d}^2 k}{A_\mathrm{BZ}} \frac{\Lambda_{k,q}\Lambda^*_{k+g,q+g}}{\Lambda_{q+g,q}\Lambda^*_{k+g,k}} v(k-q)\rho^*_{k,g}, \quad (20\mathrm{b})$$

with A_BZ the area of the original material's Brillouin zone. Here, V^H_g and $V^\mathrm{F}_{k,g}$, respectively, correspond to the Hartree and Fock potentials. We assume that they do not spontaneously break the $\mathcal{C}_n$ rotation symmetry of the system; i.e., $V^\mathrm{H}_{R_n g} = V^\mathrm{H}_g$ and $V^\mathrm{F}_{R_n q, R_n g} = V^\mathrm{F}_{q,g}$. Notice that the ratio of form factors in the Fock term is gauge invariant; its phase corresponds to the Berry flux accumulated around the momentum-space loop $(q \to k \to k + g \to q + g \to q)$. Finally, we do not consider the zero-momentum exchange terms of the interactions, as they contribute only a global constant energy shift proportional to the square of the total density. This excludes the $k = q$ part of the Fock integral, which we have made explicit using a primed integral notation.

Our goal is to find exact solutions of $H(q)$ at all high-symmetry points q_0 of the rBZ in the perturbative regime, for which the Hamiltonian can be projected onto the set of states $\{|\chi(k)\rangle | k \in \mathcal{B}(q_0)\}$ whose exact degeneracy is enforced by $\mathcal{C}_n$ symmetry (as explained in Sec. III). Similar to the noninteracting case, the projected Hamiltonian $PH(q)P$ takes the circulant form of Eq. (6) with the modified parameters

$$a_0 = \varepsilon_{q_0}, \qquad a_k = [V^\mathrm{HF}_{q_0, \ q_k - q_0} - V_{q_k - q_0}]\Lambda_{q_k, q_0}, \quad (21)$$

and the derivation of the symmetry eigenvalues in Sec. III B follows, yielding

$$\nu_p(q_0) = \left\lfloor \frac{\pi - \Phi_{q_0}^{\circlearrowleft}}{2\pi} \right\rfloor,$$

$$\Phi_{q_0}^{\circlearrowleft} = p \arg[(V_{q_1-q_0} - V_{q_0,q_1-q_0}^{\mathrm{HF}})\Lambda_{q_1,q_0}]. \quad (22)$$

However, in contrast to the noninteracting case, this equation is not sufficient to determine the symmetry eigenvalue $\nu_p(q_0)$, because the Hartree-Fock potential V^{HF} formally depends on the value of $\rho_{k,g}$ for all k in the original BZ. To make analytical progress, we now resort to an approximation, justified in the perturbative regime considered throughout this manuscript, to simplify the functional of the Hartree-Fock potential.

2. Resonant approximation

What justifies the restriction to high-symmetry points in Sec. III is that, for the weak perturbation considered, the original band structure of the material remains unchanged except in small neighborhoods around the rBZ high-symmetry points. In these small patches, there exist superlattice harmonics with momentum g that resonantly couple states of the original band with the same energy (their degeneracy is enforced by the $\mathcal{C}_n$ rotation symmetry). In other words, the state $|\chi(k)\rangle$ from the original band structure substantially hybridizes with $|\chi(k+g)\rangle$ only if k lies close enough to a high-symmetry point q_0 for which $q_0 + g \in \mathcal{B}(q_0)$. This leads to nonzero values of $\rho_{k,g} = \Lambda_{k+g,k}\langle c_{k+g}^{\dagger}c_k\rangle$ only in those regions where the superlattice potential is resonant. Our perturbative treatment holds only when the area A_{res} of resonant regions remains small compared to the total Brillouin zone area, as measured by the coefficient $\eta = A_{\mathrm{res}}/A_{\mathrm{BZ}} \ll 1$. Because of this, we can assume $\rho_{k,g}$ and the form factors appearing in the Fock integral are independent of momentum within each of the small patches of size A_{res}. Altogether, this allows one to replace the integral in the definition of $V_{q,g}^{\mathrm{HF}}$ by the sum

$$\int \frac{\mathrm{d}^2 k}{A_{\mathrm{BZ}}} \simeq \eta \sum_{(k,k+g)\in\mathcal{B}(q_0)}, \quad (23)$$

an approximation that we refer to as the "resonant approximation." We point out that this resonant approximation becomes equivalent to the few-patch model introduced in Ref. [39] when the resonance region A_{res} is assumed to be as large as the rBZ.

3. Self-consistency condition

Under the resonant approximation described above, the only order parameters $\rho_{k,g}$ appearing in the Hartree-Fock integrals involve momenta $(k, k+g) \in \mathcal{B}(q_0)$, i.e., rotated images of a high-symmetry point q_0. Thus, there exist integers α and β such that $k = R_p^{\alpha} q_0$ and $k + g = R_p^{\beta} q_0$. Using the analytic form of the lowest miniband eigenvector $|\phi_{\nu_p(q_0)}\rangle$ at q_0 derived in Eq. (8), we find

$$\rho_{k,g} = \Lambda_{k+g,k}\langle \phi_{\nu_p(q_0)}|c_{k+g}^{\dagger}c_k|\phi_{\nu_p(q_0)}\rangle$$

$$= \frac{1}{p}\Lambda_{k+g,k}\omega_p^{(\beta-\alpha)\nu_p(q_0)}. \quad (24)$$

This equation gives the order parameters appearing in the Hartree-Fock potential as a function of the symmetry eigenvalue and a finite set of form factors of the original band. In Appendix B, we combine Eqs. (23) and (24) to rewrite the Hartree-Fock potential at all high-symmetry points q as

$$V_{q,g}^{\mathrm{HF}} = \frac{\eta v(g)}{p}\omega_p^{-\nu_p(q)}\Lambda_{q,q+g}\Gamma_q^{(n)}(C_n, v, \Lambda), \quad (25)$$

where the auxiliary coefficients $\Gamma_q^{(n)}(C_n, v, \Lambda)$ depend on only the Chern number modulo n of the lowest miniband C_n, the two-body interaction potential $v(q)$, and a finite number of form factors of the original band Λ_{q_1,q_0} with both q_0 and q_1 high-symmetry points of the rBZ. The analytical expressions of the $\Gamma_q^{(n)}$ are given for all $n = 2, 3, 4, 6$ and all high-symmetry points q in Appendix B.

Equations (22) and (25) form the second main result of this paper: The topology of the (fully filled) lowest miniband can be perturbatively determined from a few form factors of the original band structure as the solution to self-consistent equations for the symmetry eigenvalues at high-symmetry points. Contrary to the noninteracting case presented in Sec. III, however, these self-consistent equations cannot be solved analytically to provide a comprehensive phase diagram akin to those from Table I. Nonetheless, because the symmetry eigenvalues can take only a finite number of values, one can solve the equations algorithmically by looping over all allowed eigenvalues and checking whether the self-consistency condition of Eq. (22) is satisfied by computing Eq. (25) using a finite number of the original material's form factors. These steps are described in Table II in the regime where the amplitude of the Hartree-Fock potential is greater than that of the externally applied superlattice, which we now investigate in more detail.

B. Interaction-driven topology

A subtle issue introduced by the resonant approximation described in the previous paragraph is the emergence of the phenomenological parameter η measuring the size of the resonant area. Fortunately, this parameter drops out in the limit where the strength of the Hartree-Fock potential dominates over the amplitude of the applied superlattice potential. In this case, we replace $V_{q,g}^{\mathrm{HF}} - V_g \simeq V_{q,g}^{\mathrm{HF}}$ in the loop phases, which gives

$$\Phi_{q_0}^{\circlearrowleft} \simeq p \arg\left[-V_{q_0,q_1-q_0}^{\mathrm{HF}}\Lambda_{q_1,q_0}\right]$$

$$= p \arg\left[-\Gamma_{q_0}^{(n)}\right] - 2\pi\nu_p(q_0) \quad (26)$$

independent of the phenomenological parameter η. This drastically simplifies the self-consistent equations, which are recast as

$$\left\lfloor \frac{\pi - p(q_0)\arg\left[-\Gamma_{q_0}^{(n)}\right]}{2\pi} \right\rfloor = 0, \qquad (27)$$

where, as in Sec. III, $p(q_0)$ denotes the largest divisor of n for which $R_n^{n/p}q_0 = q_0$. A self-consistent Hartree-Fock solution requires Eq. (27) to be simultaneously satisfied for all high-symmetry points q_0 of the rBZ.

In the limit where the superlattice potential is weak compared to the interaction scale, checking whether a self-consistent Hartree-Fock solution with Chern number C_n exists simply reduces to the computation of $\Gamma_{q_0}^{(n)}$ for all high-symmetry points q_0 of the rBZ using a few form factors Λ of the original band structure and the functional form of the two-body interaction potential $v(q)$, in order to check that Eq. (27) is satisfied. This constitutes an efficient algorithm to predict which Chern number is favored by interactions solely from the knowledge of the few form factors appearing in Eq. (B2), as summarized in Table II in the introduction. When no superlattice potential is present and when the form factors of the material do not yield any self-consistent solutions for the symmetry eigenvalues $\nu_p(q_0)$, at least one of the high-symmetry points considered remains gapless in the presence of perturbatively weak interactions. This crossing can still be opened for larger values of the interaction amplitude in the strong-coupling limit.

V. APPLICATION TO RHOMBOHEDRAL GRAPHENE MULTILAYERS

In this section, we apply our formalism to rhombohedral (also referred to as *ABC*-stacked) graphene multilayers. This choice is motivated by the recent discovery of quantum anomalous Hall effects in electrically biased penta- and hexalayer graphene subject to a superlattice potential induced on its bottom surface by a near-aligned hexagonal boron nitride (*h*-BN) substrate [36,38]. We show that the theory developed in the previous sections captures these experimental observations, providing an elegant and numerically efficient route to the topological phase diagram of the graphene N-layer stacks. We organize our discussion as follows: Sec. V A introduces the tight-binding model used in our calculations; Sec. V B applies the noninteracting theory in Sec. III and highlights that the effect of the substrate-induced superlattice potential decreases exponentially fast as a function of the bias applied across the sample; Sec. V C includes the effects of interactions using the methodology given in Sec. IV to obtain the Hartree-Fock phase diagram of the material; finally, Sec. V D shows that quantum anomalous Hall behaviors are primarily induced by the Fock contribution, allowing us to analytically predict the range of moiré lattice constants yielding

quantum anomalous Hall behaviors for the different rhombohedral N-layer graphene stacks.

A. Model

To describe rhombohedral N-layer graphene, we use the tight-binding model developed in Ref. [53] with the effect of a displacement field included as a layer-dependent potential energy $E_\ell = E_z[\ell - (N-1/2)]$ with $\ell = 0, \ldots, N-1$ denoting the layer index. All results presented in this section are obtained using the tight-binding coefficients from Ref. [46]; the results only minimally change with other choices of tight-binding coefficients [33,54–56]. We also include in the band structure the uniform energy shift experienced by the atoms closest to the nearly aligned h-BN due to virtual second-order tunneling processes. As derived in Ref. [57], this effect can be described by a potential $V_0 P$ with $V_0 = 29$ meV, where P denotes the projection onto the B sublattice of the bottom layer (i.e., on the atoms
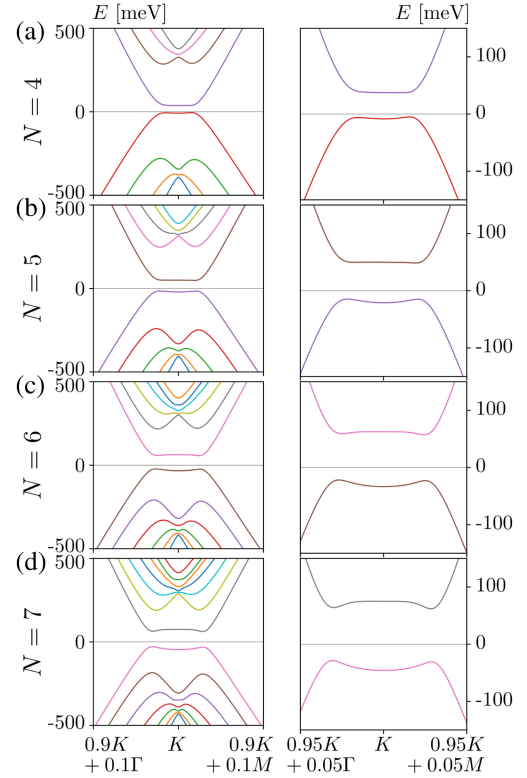

FIG. 1. Band structure of rhombohedral N-layer graphene along the $\Gamma - K - M$ line near the K point, computed with the tight-binding model from Refs. [46,53] with a displacement field corresponding to $E_z = 25$ meV and a uniform potential on the bottom layer $V_0 = 29$ meV derived in Ref. [57]. (a)–(d) correspond to different numbers of layers N as indicated on the left. They feature a broadened view of the band structure (left) where all bands of the tight-binding model are visible along the line $(0.9K + 0.1\Gamma) \rightarrow K \rightarrow (0.9K + 0.1M)$ and a close-up near charge neutrality (right) along the path $(0.95K + 0.05\Gamma) \rightarrow K \rightarrow (0.95K + 0.05M)$.
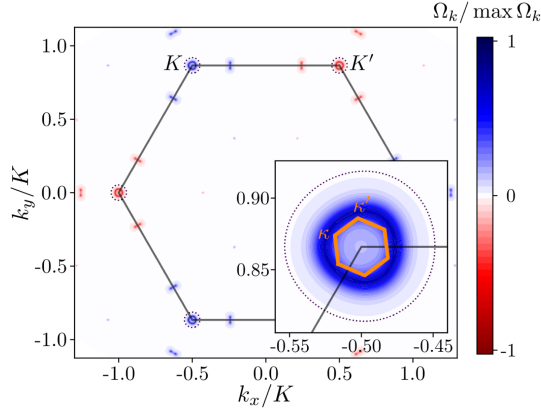
FIG. 2. The single-band formalism in Secs. III and IV applies only in the small regions in momentum space where the lowest conduction band of rhombohedral N-layer graphene exhibits an indirect gap to higher bands. These regions are encircled by a dashed line for the specific case of $N = 5$ in the presence of a displacement field $E_z = 25$ meV. The regions span only a small fraction of the graphene stack's BZ (black line) near the K and K' points but, nevertheless, contain most of the Berry curvature (color scale, also computed for $N = 5$ and $E_z = 25$ meV), which is concentrated in rings around those points—see the inset. The lattice mismatch and twist of the substrate fixes the position of the corners κ and κ' of the folded rBZ, represented by a thick orange line for a twist of 0.7° and lattice mismatch corresponding to graphene on h-BN.

closest to the substrate after inclusion of lattice relaxation effects):

$$[P]_{(\ell,\tau),(\ell',\tau')} = \delta_{\ell,\ell'}\delta_{\tau,\tau'}\delta_{\ell,0}\delta_{\tau,B}, \tag{28}$$

with $\tau \in \{A, B\}$ labeling the sublattice index. In Fig. 1, we show the band structure of N-layer rhombohedral graphene around the K point, where the gap at charge neutrality is smallest, with $E_z = 25$ meV and $N = 4, \ldots, 7$.

One requirement for the band-projected formalism of the previous sections to apply is that the conduction band of the N-layer graphene stack be isolated throughout the reduced Brillouin zone set by the superlattice potential. As can be seen in Fig. 1, an indirect band gap between the lowest and higher conduction bands exists only in a narrow region near the K point. This is the small area on which we now focus to apply the results derived in Secs. III and IV. To better visualize this narrow region of interest, we represent the full Brillouin zone of rhombohedral pentalayer ($N = 5$) graphene in Fig. 2 and encircle with dashed lines the points where its lowest conduction band remains below the minimum of the second conduction band for $E_z = 25$ meV. The inset in Fig. 2 shows that this single-band regime applies to only momenta $k = K + q$ distant from the graphene's stack K point by at most $|q/K| \simeq 0.04$. Similar boundaries are obtained for $N = 4, \ldots, 7$ so long as $E_z \leq 50$ meV. While the identified single-band regime spans only a tiny fraction of the N-layer original Brillouin zone, it proves to be relevant

for the experiments of Refs. [36,38], as we now explain: The nearly aligned h-BN substrate imposes a superlattice potential on the graphene stack whose periodicity and orientation are determined by the lattice mismatch $\epsilon = 0.0163$ between graphene and h-BN and the relative twist angle θ between them. We determine where the κ corner of the superlattice rBZ is located within graphene's BZ from these factors using $\kappa = K - (1/1 + \epsilon)R(\theta)K$, where $R(\theta)$ denotes the rotation by angle θ [46]. We later present results as a function of the location of κ, which is a way of parametrizing the superlattice periodicity and orientation. In Ref. [36], the twist angle $\theta \simeq 0.7°$ implies a superlattice period $a_{super} \simeq 11.5$ nm corresponding to corners of the rBZ at a relative distance $|\kappa/K| \simeq 0.02$ from the pentalayer K point. The rBZ obtained for these values is depicted with a thick orange line in the inset in Fig. 2.

Figure 2 also shows the Berry curvature of the lowest conduction band of pentalayer graphene when $E_z = 25$ meV, which is concentrated in a small ring around the K point, entirely contained within the single-band regime. There are additional peaks of Berry curvature induced by trigonal warping along the $K - M$ and $K - \Gamma$ lines far beyond the identified region of interest; hence, these do not play a substantial role in our story.

B. Substrate-induced topology

In the experiments in Refs. [36,38], the quantized anomalous Hall effect has been observed only for displacement fields polarizing the electronic wave functions of the conduction band on the layer located furthest away from the h-BN substrate giving rise to the superlattice potential. In our notation, this can be modeled with a positive displacement field $E_z > 0$ and a long-wavelength potential that couples to only the bottom layer $\ell = 0$ [58]. In fact, the effect of the potential on the B sublattice of the bottom layer alone (i.e., on the carbon atoms of the bottom graphene sheet with no direct vertical neighbor in the second layer) is found sufficient to capture the full effect of the h-BN substrate on the bottom of the conduction band in the experimentally relevant range of displacement fields [46].

We, therefore, include the effect of the substrate as follows. First, the lattice mismatch and twist of the substrate fix the corners κ and κ' of the rBZ, represented by a thick orange line in Fig. 2. Then, the superlattice potential induced by the substrate is introduced as

$$V_{h-BN}(r) = -P\sum_g V_g e^{ig \cdot r}, \tag{29}$$

with P representing the projection onto the B sublattice of the bottom layer [see Eq. (28)]. This internal structure of the potential does not change the form of the band-projected Hamiltonian appearing in Eq. (3) nor the derivation presented in Sec. III provided we use layer and sublattice weighted form factors

$$\Lambda^{\mathrm{ls}}_{q',q} = \langle \chi(q') | P | \chi(q) \rangle \qquad (30)$$

instead of the bare form factors of the conduction band. Finally, we consider only the lowest harmonics of the superlattice, which are equal for the three $\mathcal{C}_3$ related harmonics $g_1 = \kappa + \kappa'$, $g_2 = \kappa - 2\kappa'$, and $g_3 = -2\kappa + \kappa'$. We adopt the notation introduced in Table I ($n = 3$ column) and write $V_{g_{1,2,3}} = |V| e^{i\theta}$. For consistency with the V_0 used in the tight-binding calculation, we use the values $|V| = 21$ meV and $\theta = 196.6°$ from Ref. [57].

To draw the noninteracting topological phase diagram of the N-layer graphene stacks, we vary the displacement field E_z in the experimentally relevant range 0–40 meV and use the expression for the Chern number modulo three C_3 from Table I (see also Appendix A). We choose κ as illustrated in Fig. 2, which corresponds to a $\theta = 0.7°$-twisted h-BN substrate. Our results, shown in Fig. 3 (a_1) for $N = 5$, 6, and 7, agree with the expected behavior of rhombohedral graphene in the absence of interactions [59]: We observe a transition from a trivial $C_3 = 0$ insulator to a topological state with $C_3 = N$ (mod 3) as E_z increases above a threshold approximately given by $E_z \simeq V_0/(N-1)$ [46] for which a topological gap closing at the rBZ center (γ) occurs.

To understand the physical relevance of this result, we also evaluate the noninteracting gap $\Delta = \min(\Delta_\kappa, \Delta_{\kappa'})$, where Δ_{q_0}, the gap opened by the superlattice at the high-symmetry point q_0, is determined using Eq. (10) to find the energy difference between the lowest two minibands at each high-symmetry point. We plot this gap in Fig. 3 (a_2), where we observe that Δ rapidly decays as the displacement field E_z increases. This is a consequence of the projector appearing in Eq. (30). Indeed, the displacement field polarizes the conduction band on the layer located furthest away from the one where the superlattice potential acts, which decreases the amplitude of the layer and sublattice weighted form factor $\Lambda^{\mathrm{ls}}_{R_3\kappa,\kappa}$. In fact, it is known that, near the K point of the N-layer graphene, the weights of the conduction band's wave functions on the $\ell = 0$ layer decrease exponentially fast with E_z [53], which explains the exponential decay of the gap Δ_κ in Fig. 3 (a_2). We emphasize that the topological transitions in Fig. 3 (a_1) are associated with a gap closing between the valence and conduction bands at γ and, therefore, do not lead to a vanishing value of $\Delta = \min(\Delta_\kappa, \Delta_{\kappa'})$, which measures the gap to higher conduction bands.

C. Interaction-induced topology

To summarize this noninteracting calculation, we have found that the presence of the nearly aligned h-BN substrate yields, for sufficiently large E_z, a topological lowest miniband with Chern number consistent with $C_3 = N$ (mod 3), whose gap to higher conduction bands decreases exponentially as the displacement field E_z grows due to the
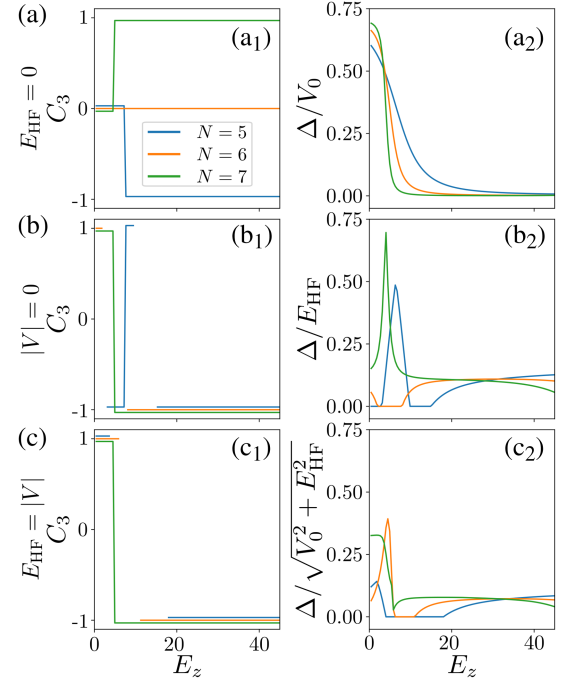

FIG. 3. Perturbative phase diagrams of rhombohedral N-layer graphene as a function of the applied displacement field for different interaction strength $E_{\mathrm{HF}} = 0$ (a), in the absence of superlattice potential $|V| = 0$ (b), and for $E_{\mathrm{HF}} = |V|$ (c). The left panels (subscript 1) show the Chern number of the lowest conduction band, obtained with the noninteracting formalism in Sec. III for (a) and the self-consistent Hartree-Fock calculation in Sec. IV in (b) and (c). In (b) and (c), the absence of lines indicates that no perturbative self-consistent solution exists, leading to metallic behavior. The right panels (subscript 2) show the gap opened by the superlattice.

polarization of the conduction band in the layer furthest away from the substrate. In particular, this exponential suppression suggests that the noninteracting approximation breaks down for large E_z and that the dominant gap at κ is mostly induced by interaction effects—to which we now turn.

To find the topological character of the lowest conduction band for large displacement fields, we momentarily turn off the superlattice potential ($|V| = 0$) and include the effects of interactions within the Hartree-Fock approximation. Following the method summarized in Table II and derived in Sec. IV, we determine the Chern number C_3 of the lowest conduction band in the rBZ for which a perturbative self-consistent Hartree-Fock solution exists.

We display the resulting purely-interacting Hartree-Fock phase diagrams in Fig. 3(b) for the same choice of κ as in Fig. 3(a) (see the inset in Fig. 2). For all considered values of E_z and N, we find at most one C_3 value for which a self-consistent Hartree-Fock solution exists using our algorithm. When no such C_3 is found, our perturbative Hartree-Fock calculation predicts a metallic state. These metallic regions, mostly found at intermediate values of the displacement field $E_z \sim 5$–10 meV, appear in Fig. 3 (b_1) as

domains with no data points (the Chern number is not defined for gapless states) corresponding to vanishing-gap regions in Fig. 3 (b_2).

The main feature of this purely interacting calculation is the presence of a topological insulator with $C_3 = -1$ at large $E_z > 15$ meV for all N considered in Fig. 3. This correctly captures the experimental observation of the quantized anomalous Hall effect at integer filling of the moiré h-BN/rhombohedral graphene systems in Refs. [36,38]. Finally, we comment that the gap closing at γ remains visible in the $N = 5$ and $N = 7$ interacting phase diagram as a topological transition for which Δ does not vanish (see the discussion above). We observe that the two excited states above κ cross at these transition points, leading to a cusp in the gap depicted at Fig. 3(b_2).

To obtain a complete picture intertwining the noninteracting results of Fig. 3(a) and the Hartree-Fock insights of Fig. 3(c), we reintroduce the superlattice potential ($|V| > 0$) and use the full-fledged Eq. (22) to draw the perturbative Hartree-Fock phase diagrams of the rhombohedral N-layer graphene stacks as a function of the displacement field. This requires us to introduce a phenomenological parameter $E_{\mathrm{HF}} = \eta v(g_\kappa)$ measuring the strength of the Hartree-Fock potential built up within the small resonant regions described in Sec. IV A. With $\varepsilon = 6$, we estimate this parameter to be equal to $(E_{\mathrm{HF}}/|V|) \sim (e^2/4\pi\varepsilon_0\varepsilon a_{\mathrm{super}}|V|) \simeq 1$ and show the results obtained for this realistic value in Fig. 3(b). For $E_z > 20$ meV, the results almost perfectly agree with the purely interacting case displayed in Fig. 3(c), while the interacting and noninteracting contribution are similar in magnitude and compete for smaller displacement fields.

We stress that our perturbative calculation does not aim to quantitatively account for all experimental features. Rather, its intent is to rapidly sketch the phase diagram of a particular material using a few material-specific coefficients. In the case of rhombohedral N-layer graphene, these coefficients are the form factors Λ and layer-sublattice weighted form factors Λ^{ls}. With only a handful of these coefficients, we are able to qualitatively capture the phases observed in the experiments in Refs. [36,38].

D. Fock term and analytical insights

We now seek additional insight into the nontrivial topology in the experimentally relevant regime of large displacement field $E_z > 25$ meV, where the effect of the superlattice potential is negligible compared to the Hartree-Fock corrections. To this aim, we consider the purely interacting case $|V| = 0$ and compare the Chern number of the lowest miniband when we include both Hartree and Fock terms or only one of the two. These Chern numbers, obtained by the algorithm derived in Sec. IV B, are displayed in Fig. 4 for $N = 3, \ldots, 8$ and $E_z = 30$ meV as a function of the position of the κ corner of the rBZ respective to the graphene stack's K point. We show only results within the single-band regime identified in Sec. V A, i.e., for $|\kappa| \leq 0.04|K|$. For the sake of concreteness, we indicate with black crosses the special points corresponding to the rBZ corner κ set by an h-BN substrate with a twist angle $\theta = 0°, 0.5°, 1°, 1.5°$, and $2°$.

The first line in Fig. 4 corresponds to the full Hartree-Fock results and efficiently predicts for which values of N the rhombohedral stack exhibits a topological band under
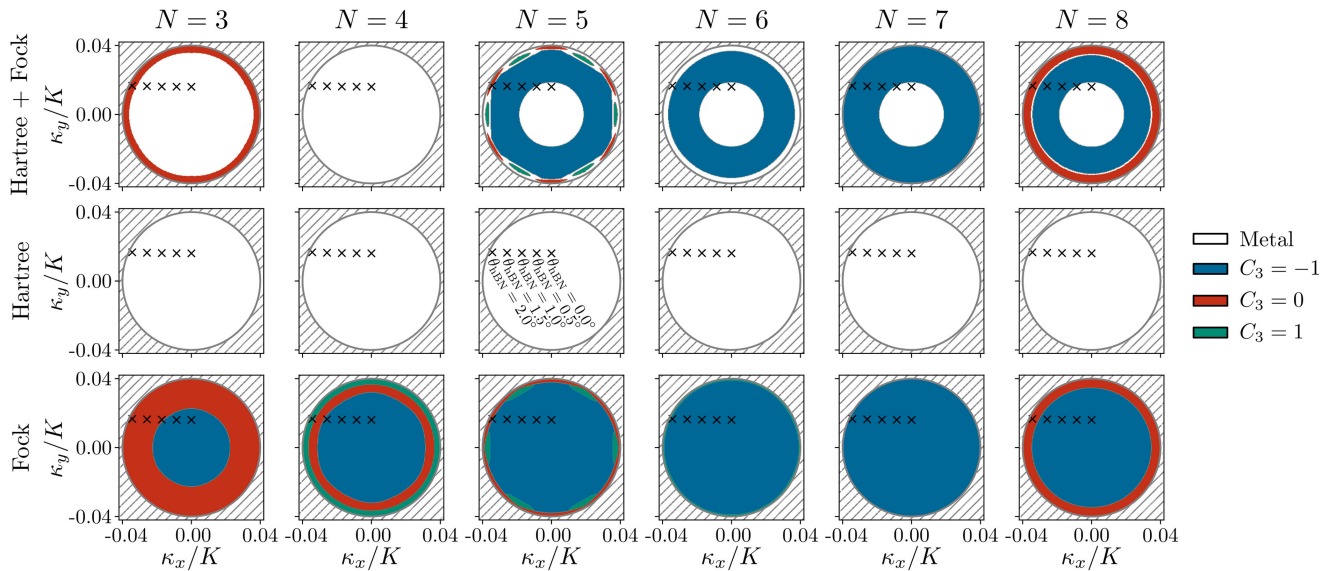
FIG. 4. Hartree-Fock (top row), Hartree (middle row), and Fock (bottom row) purely interacting phase diagram of rhombohedral N-layer graphene for $N = 3, \ldots, 8$ (different columns) and $E_z = 30$ meV as a function of the position of the κ corner of the rBZ relative to the graphene stack's K point. The black crosses represent the value of κ corresponding to the rBZ corner set by an h-BN substrate with a twist angle $\theta = 0°, 0.5°, 1°, 1.5°$, and $2°$, as indicated in the middle row of the $N = 5$ column.

large bias. All rhombohedral stacks feature a metallic phase for small mismatch $|\kappa/K|$, where no self-consistent Hartree-Fock solutions can be found, and insulating phases for larger $|\kappa/K|$. The exact value of $|\kappa/K|$ at which the transition between the metallic and insulating phases occur and the Chern number of the insulating phase vary depending on the number of layers N. For instance, the transition occurs for κ outside of the single-band regime for $N = 4$. There is, nevertheless, a striking similarity between all multilayers with $N \geq 5$: The first insulating state appears for $|\kappa/K| \simeq 0.02$ and has Chern number $C_3 = -1$. In particular, all $N \geq 5$ rhombohedral stacks should feature quantum anomalous Hall behavior under large biases when the rBZ is set by an h-BN substrate with a twist angle $\simeq 1°$. Our results may also explain why, to this date, quantum anomalous Hall behaviors were observed in penta- and hexalayer graphene but not in quadrilayer graphene.

Comparing the full Hartree-Fock solutions to those obtained by considering only the Hartree (second line in Fig. 4) and Fock (third line in Fig. 4) corrections, we observe that the Hartree term always favors a metallic phase, while the Fock term gives rise to self-consistent insulating states and, in particular, to those with nonzero Chern number. From Fig. 4, it hence appears that the Hartree contribution dominates for small κ, leading to a metallic state in the full-fledged solution, while the Fock terms take over for $|\kappa/K| \geq 0.02$.

To qualitatively understand the competition between the Hartree and Fock terms, let us simplify the equations in Sec. IV B under the assumptions that (i) the particles interact through a short-range interacting potential such that $v(\kappa) \simeq v(g_\kappa)$; (ii) the band structure of the N-layer graphene can be reduced to the two-band model with continuous rotation symmetry of Ref. [59],

$$\mathcal{H}_{\mathrm{eff}}(k) = \begin{bmatrix} \Delta & \frac{v_F^N}{t_1^{N-1}}(k_x - ik_y)^N \\ \frac{v_F^N}{t_1^{N-1}}(k_x + ik_y)^N & -\Delta \end{bmatrix}, \quad (31)$$

parametrized by the displacement field $\Delta = E_z(N-1)/2$, graphene's Fermi velocity $v_F = 550$ meV.nm, and the tunneling $t_1 = 360$ meV between nearest interlayer neighbors [46]; and (iii) the ratio of form factors $\Lambda_{k,q}\Lambda_{q+g,k+g}/\Lambda_{q+g,q}\Lambda_{k,k+g}$ appearing in the Fock term can be approximated by a phase factor equal to the integrated flux of Berry curvature contained in the $(q \to k \to k + g \to q + g \to q)$ loop discussed below Eq. (20). Under these approximations, we can intuitively understand why the Fock term is negligible for small κ and eventually dominates over the Hartree term for $|\kappa/K| \sim 0.02$–0.03, where it drives the system toward an insulator with nonzero Chern number $C_3 = -1$. To see this, we use approximations (i)–(iii) to rewrite the Γ factors of Eq. (B2) as

$$\Gamma_{\kappa/\kappa'}^{(3)} \simeq 1 + \omega_3^{C_3}(1 - e^{i\phi_{\mathrm{F}}}), \qquad \phi_{\mathrm{F}} = \int_{\mathcal{L}_\kappa} d^2k\,\Omega_k, \quad (32)$$

with $\mathcal{L}_\kappa$ denoting the region enclosed in momentum-space loop $(\kappa \to \kappa' \to \kappa' + g_\kappa \to \kappa + g_\kappa \to \kappa)$ and where the Berry curvature expanded to leading order in k reads [46]

$$\Omega_k = \frac{N^2}{2}\frac{v_F^2}{\Delta^2}\left(\frac{v_F|k|}{t_1}\right)^{2(N-1)}. \quad (33)$$

While we do not have an analytic formula for the integrated Berry flux ϕ_{F}, it is straightforward to integrate Ω_k in a circle of radius $|\kappa|$. Then, to estimate the critical κ where the Fock term exceeds the Hartree term, we write ϕ_{F} as the flux threading this circle scaled by a factor $\xi_\kappa \sim 1$ that we have to numerically evaluate:

$$\phi_{\mathrm{F}} = \frac{\pi\xi_\kappa N^2}{2}\frac{t_1^2}{\Delta^2}\left[\frac{v_F|\kappa|}{t_1}\right]^{2N}. \quad (34)$$

For all the κ and N considered, we find ξ_κ to be contained between one-half and one.

For $\kappa = 0$, the momentum-space loop discussed above is reduced to a point such that the Berry flux $\phi_{\mathrm{F}} = 0$, resulting in a vanishing the Fock contribution $(1 - e^{i\phi_{\mathrm{F}}}) = 0$. This leaves only a Hartree term in $\Gamma_{\kappa/\kappa'}^{(3)} = 1$, which does not yield any self-consistent solutions [as can be straightforwardly checked with Eq. (27)]. This explains the dominance of the Hartree term and the metallic phase at small κ for all N; see Fig. 4. As $|\kappa|$ increases, the system eventually reaches a point where $\phi_{\mathrm{F}} = \pi/3$, for which the equations (27) display their first self-consistent solution, which has Chern number $C_3 = -1$ as can be straightforwardly checked from Eq. (32). Approximating $\xi_\kappa \simeq 0.5$ for the sake of concreteness, the transition occurs for

$$\frac{|\kappa^*|}{K} \simeq \frac{t_1}{v_F K}\left[\frac{(N-1)E_z}{\sqrt{3}Nt_1}\right]^{1/N}, \quad (35)$$

which is contained between 0.020 and 0.026 for $N = 5, …, 8$. These values all belong to the $C_3 = -1$ insulating phase observed in Fig. 4 for $N \geq 5$.

The exceptional coincidence is that this very specific range, $0.020 < |\kappa^*|/K < 0.026$, exactly matches the size of the rBZ imposed by an h-BN substrate twisted by about one degree—see crosses in Fig. 4. According to our perturbative insights, this coincidence between the h-BN–graphene mismatch and the value of $0.6t_1/(v_F K)$ is the main reason for observing quantum anomalous Hall behaviors in rhombohedral graphene stacks, where the numerical factor 0.6 comes from the term raised to a power $1/N$ in Eq. (35) that lies between 0.5 and 0.7 for $N = 5, …, 8$.

VI. CONCLUSION AND OUTLOOK

We have developed a highly versatile and computationally inexpensive method for predicting the topological properties of materials or heterostructures subjected to a superlattice potential by combining degenerate perturbation theory with the symmetry indicators method. Our analysis applies to externally imposed superlattices, for which we provide a systematic rule to find the Chern number of the superlattice-induced miniband from the harmonics of the superlattice potential and a few material-specific coefficients, as well as to interaction-induced potentials, for which we derive an efficient algorithm to determine all Chern numbers compatible with a self-consistent solution to the Hartree-Fock equations. Our approach correctly captures the phases observed in rhombohedral graphene multilayers [36,38] and, importantly, offers a unique analytical insight as to why the quantum anomalous Hall effect emerges in these systems.

While our main emphasis here was to apply the perturbative symmetry indicator method to superlattice materials, it can straightforwardly be extended to twisted homobilayers. In particular, in Appendix C, we show that it accurately reproduces the topological phase diagram of the continuum model for twisted transition metal dichalcogenide homobilayers [12,13] and of twisted bilayer graphene in the chiral limit where the topology of the bands around zero energy is fully characterized by Chern numbers [60]. In the future, we plan to develop a similar framework to obtain additional topological quantum numbers, such as mirror-Chern or $\mathbb{Z}_2$ invariant, for which symmetry indicator formulas are available [61–63].

APPENDIX A: NONINTERACTING CHERN NUMBER FOR ALL n

In this appendix, we combine Eqs. (11) and (18) to populate the summary given in Table I. For simplicity, we treat the $n = 2, 3, 4, 6$ cases separately.

1. $n = 2$

In the case $n = 2$, the rectangular BZ possesses four high-symmetry points with point symmetry group $\mathcal{C}_2$, conventionally named γ, x, y, and m. They are graphically defined in the second row in Table I, where we also show the harmonics of the potential $V_{q=x,y,m}$ connecting the high-symmetry points x, y, and m to their respective R_2-rotated images. Since x, y, and m are not related by any symmetries, $V_{x,y,m}$ are independent degrees of freedom.

Following Sec. III B, the Chern number of the lowest superlattice-induced miniband can be entirely determined from the three harmonics $V_{q=x,y,m}$ and the four matrix elements $\langle q|U_2|q\rangle$, with $q \in \{\gamma, x, y, m\}$ and U_2 the representation of the R_2 rotation acting on the Bloch vectors. Specifically, using Eq. (12), each high-symmetry point q defines an independent loop phase

$$\Phi_{q=x,y,m}^{\circlearrowleft} = 2\arg\left[V_{g_q}\frac{\langle q|U_2|q\rangle^*}{\langle \gamma|U_2|\gamma\rangle^*}\right]. \quad (A1)$$

In terms of these variables, Eqs. (11) and (18) yield

$$C_2 = \sum_{q=x,y,m}\left\lfloor\frac{\pi - \Phi_q^{\circlearrowleft}}{2\pi}\right\rfloor \quad (\text{mod } 2), \quad (A2)$$

giving the phase diagram in the last row in Table I.

In the limit where the period of the superlattice is long, we use Eq. (15) to simplify the expression of the $\Phi_2^{\circlearrowleft}(q)$ phases. The loop $q \to R_2q \to R_2^2q = q$ does not enclose any area (second line in Table III), which results in $\Phi_2^{\circlearrowleft}(q) = 2\arg V_{g_q}$. Furthermore, since $p = 2$ is even for the relevant high-symmetry points, the potential V_{g_q} is real, such that $\arg V_{g_q} \in \{0, \pi\}$ and $\lfloor(\pi - \Phi_2^{\circlearrowleft}(q))/2\pi\rfloor = -\arg V_{g_q}/\pi$. When plugged into Eq. (A2), this gives

$$C_2 = -\sum_{q=x,y,m}\frac{\arg V_{g_q}}{\pi} = \frac{\arg(V_{g_x}V_{g_y}V_{g_m})}{\pi} \quad (\text{mod } 2), \quad (A3)$$

using $x = -x(\text{mod } 2)$. We can rewrite this as

$$C_2 = \Theta(-V_{g_x}V_{g_y}V_{g_m}) \quad (\text{mod } 2), \quad (A4)$$

which is quoted in the fourth line in Table I. Thus, in the long-period limit, the lowest superlattice-induced miniband necessarily has nontrivial topology when an odd number of the harmonics $(V_{g_x}, V_{g_y}, V_{g_m})$ are negative.

2. $n = 3$

In the case $n = 3$, the hexagonal BZ possesses three high-symmetry points with point group $\mathcal{C}_3$ named γ, κ, and κ' and graphically represented in the second line in Table I (third column), together with the harmonics V_{g_κ} and $V_{g_{\kappa'}}$ connecting the high-symmetry points κ and κ' to their respective R_3-rotated images. Since the superlattice potential is real and $\mathcal{C}_3$ symmetric, these two elements are complex conjugates, $V_{g_{\kappa'}} = V_{g_\kappa}^*$. As a result, the Chern number of the lowest superlattice-induced miniband is completely determined by $V_{g_\kappa} = |V|e^{i\theta}$ and the three matrix elements $\langle q|U_3|q\rangle$, with

$q \in \{\gamma, \kappa, \kappa'\}$, where we recall that U_3 denotes the representation of the R_3 rotation acting on the Bloch vectors. Combining these variables into the two independent loop phases [Eq. (12)]

$$\Phi_{\kappa/\kappa'}^{\circlearrowleft} = \pm 3\theta + 3 \arg\left[\frac{\langle \kappa/\kappa'|U_3|\kappa/\kappa'\rangle^*}{\langle \gamma|U_3|\gamma\rangle^*}\right], \quad \text{(A5)}$$

with the $+$ sign corresponding to κ, the Chern number in Eq. (18) can be written as

$$C_3 = \sum_{q=\kappa/\kappa'} \left\lfloor \frac{\pi - \Phi_q^{\circlearrowleft}}{2\pi} \right\rfloor \quad (\text{mod } 3), \quad \text{(A6)}$$

giving the general phase diagram in the last row in Table I. In the limit where the period of the superlattice is long, we use Eq. (15) to simplify the expression of the $\Phi_3^{\circlearrowleft}(q)$ phases. The loop $q \to R_3 q \to R_3^2 q \to R_3^3 q = q$ encloses half of the reduced Brillouin zone, as described by the $p = 3$ line in Table III. The loop phases, therefore, carry an explicit dependence on the Berry flux ϕ_B of the original material threading the rBZ, which gives the relation

$$C_3 = \sum_{\epsilon=\pm 1} \left\lfloor \frac{\pi - \frac{1}{2}\phi_B + 3\epsilon\theta}{2\pi} \right\rfloor \quad (\text{mod } 3). \quad \text{(A7)}$$

This formula is reproduced in the fourth row in Table I.

3. $n = 4$

The high-symmetry points and relevant potential harmonics for the $n = 4$ case are shown in the second row in Table I (fourth column). The main difference compared to the $n = 2$ case is that x and y are now related by $\mathcal{C}_4$ symmetry, so that there is a single relevant harmonic V_{g_x} that enters the Chern number calculation. It connects both x to its R_2 rotation and m to its R_4-rotated image [recall that below Eq. (10) we assume $a_2 = 0$, which means that no harmonic couples m to $R_2 m$]. Thus, the Chern number is entirely determined by one harmonic V_{g_x} of the superlattice potential and three matrix elements, or two independent loop phases:

$$\Phi_x^{\circlearrowleft} = 2 \arg\left[V_{g_x} \frac{\langle x|U_4^2|x\rangle^*}{\langle \gamma|U_4^2|\gamma\rangle^*}\right],$$

$$\Phi_m^{\circlearrowleft} = 4 \arg\left[V_{g_x} \frac{\langle m|U_4|m\rangle^*}{\langle \gamma|U_4|\gamma\rangle^*}\right], \quad \text{(A8)}$$

following Eq. (12), with U_4 the representation of the R_4 rotation that acts on the Bloch vectors. In terms of these variables, combining Eqs. (11) and (18) yields

$$C_4 = 2 \left\lfloor \frac{\pi - \Phi_2^{\circlearrowleft}(x)}{2\pi} \right\rfloor + \left\lfloor \frac{\pi - \Phi_4^{\circlearrowleft}(m)}{2\pi} \right\rfloor \quad (\text{mod } 4), \quad \text{(A9)}$$

from which the phase diagram in the last row in Table I is derived. The $n = 4$ case is the first for which n is not prime, allowing some high-symmetry points (here, x) to have a smaller point group symmetry than γ. This difference is the reason for the factor of 2 in the first term of the right-hand side in Eq. (A9).

In the limit where the period of the superlattice is long, we use Eq. (15) to simplify the expression of the loop phases. Only the loop connecting $m \to R_4 m \to R_4^2 m \to R_4^3 m \to m$ encloses the full rBZ and receives a Berry flux contribution of ϕ_B. Furthermore, the potential V_{g_x} is real, because $n = 4$ is even, which further simplifies the loop phases using Eq. (16). Altogether, this leads to the long-period formula

$$C_4 = \left\lfloor \frac{\pi - \phi_B}{2\pi} \right\rfloor \quad (\text{mod } 4), \quad \text{(A10)}$$

quoted in the fourth line in Table I. Note that the sign of V_{g_x} has disappeared in the long-period limit for $n = 4$. The physical origin of this observation is that, for a square lattice, flipping the sign of V_{g_x} is equivalent to shifting the origin of the system by half of either of the two Bravais lattice vectors of the superlattice potential. The sign of V_{g_x} is, therefore, purely conventional and does not influence the physics of the minibands.

4. $n = 6$

We finally turn to $n = 6$, for which the hexagonal Brillouin zone possesses three high-symmetry points γ, κ, and m defined in the second line in Table I (last column). The only relevant harmonic $V_{g_\kappa} = V_{g_m}$ (see Table I) is real, because $n = 6$ is even. As a result, the Chern number of the lowest superlattice-induced miniband only is completely determined by a single real harmonics V_{g_κ} and by three matrix elements combined into the two independent loop phases

$$\Phi_\kappa^{\circlearrowleft} = 3 \arg\left[V_{g_\kappa} \frac{\langle \kappa|U_6^2|\kappa\rangle^*}{\langle \gamma|U_6^2|\gamma\rangle^*}\right],$$

$$\Phi_m^{\circlearrowleft} = 2 \arg\left[V_{g_\kappa} \frac{\langle m|U_6^3|m\rangle^*}{\langle \gamma|U_6^3|\gamma\rangle^*}\right], \quad \text{(A11)}$$

with U_6 the representation of the R_6 rotation acting on the Bloch vectors. In terms of these variables,

$$C_6 = 3 \left\lfloor \frac{\pi - \Phi_m^{\circlearrowleft}}{2\pi} \right\rfloor + 2 \left\lfloor \frac{\pi - \Phi_\kappa^{\circlearrowleft}}{2\pi} \right\rfloor \quad (\text{mod } 6), \quad \text{(A12)}$$

which yields the phase diagram in the last row in Table I. In the limit where the period of the superlattice is long, we use Eq. (15) to simplify the expression of loop phases. Only the loop defined by κ and its R_3 rotations encloses a nonzero area and receives a contribution from the Berry

curvature of the underlying material. We also use Eq. (16) to simplify the loop phases, because V_{g_κ} is real. After some algebra, we obtain the long-period formula

$$C_6 = \Theta(-V_{g_\kappa}) + 2\left\lfloor \frac{\pi\Theta(V_{g_\kappa}) - \frac{1}{2}\phi_B}{2\pi} \right\rfloor \quad (\text{mod } 6), \quad (\text{A13})$$

given in the fourth line in Table I.

APPENDIX B: HARTREE-FOCK POTENTIAL IN THE RESONANT APPROXIMATION

In this appendix, we derive the expression for the Hartree-Fock potential at high-symmetry points given in Eq. (25) and give explicit expressions for the auxiliary variables $\Gamma_q^{(n)}$ appearing in this equation for all $n = 2, 3, 4, 6$ and all high-symmetry points q.

Let us start by considering the $n = 2$ case. We pick a high-symmetry point of the rBZ $q \in \{x, y, m\}$ and define $g_q = R_2 q - q$ as the harmonic appearing in Eq. (22). From the figure depicting the high-symmetry points in Table I, we can see that the only resonant order parameter ρ_{k,g_q} is the one with $k = q$. The latter does not appear in the Fock term [see the definition of the primed integral below Eq. (20)]. Thus, the only nonzero contribution to V_{q,g_q}^{HF} comes from the Hartree term. Using Eq. (24), this contribution reads

$$V_{q,g_q}^{\text{HF}} = \frac{\eta v(g_q)}{2} \omega_2^{-\nu_2(q)} \Lambda_{q,R_2 q}, \quad (\text{B1})$$

consistent with the general form given in Eq. (25) with

$$\Gamma_q^{(2)} = 1, \qquad q \in \{x, y, m\}. \quad (\text{B2})$$

For $n = 3$ and for each of the $q \in \{\kappa, \kappa'\}$, we define $g_q = R_3 q - q$ as in Table I. This time, there are two resonant order parameters ρ_{k,g_q}: The first is $k = q$ and appears only in the Hartree term, while the second is $k = \kappa'$ (respectively, $k = R_3^{-1}\kappa$) for $q = \kappa$ (respectively, $q = \kappa'$) and appears in both the Hartree and Fock integrals. The first contributes a term equal to unity to $\Gamma_q^{(3)}$, as in the $n = 2$ case. The second leads to the term proportional to $\omega_3^{C_3}$, as can be seen from the relation $\nu_3(\kappa) + \nu_3(\kappa') = C_3$ [Eq. (18)] and the symmetry eigenvalues appearing in the analytic expression of the order parameter [Eq. (24)]. Using the $\mathcal{C}_3$ symmetry of the form factors and the continuous rotation symmetry of the interaction kernel $v(q)$, these $k \neq q$ contributions lead to the final result

$$\Gamma_\kappa^{(3)} = 1 + \omega_3^{C_3} \frac{\Lambda_{\kappa',\ \kappa'+g_\kappa}}{\Lambda_{\kappa,\kappa+g_\kappa}}$$

$$\times \left[1 - \frac{v(\kappa' - \kappa)}{v(g_\kappa)} \frac{\Lambda_{\kappa',\kappa}\Lambda_{\kappa+g_\kappa,\ \kappa'+g_\kappa}}{\Lambda_{\kappa+g_\kappa,\kappa}\Lambda_{\kappa',\kappa'+g_\kappa}} \right],$$

$$\Gamma_{\kappa'}^{(3)} = 1 + \omega_3^{C_3} \frac{\Lambda_{\kappa,\kappa+g_\kappa-g_{\kappa'}}}{\Lambda_{\kappa',\kappa'+g_{\kappa'}}}$$

$$\times \left[1 - \frac{v(\kappa' - \kappa)}{v(g_\kappa)} \frac{\Lambda_{\kappa+g_\kappa-g_{\kappa'},\kappa'}\Lambda_{\kappa'+g_{\kappa'},\kappa+g_\kappa}}{\Lambda_{\kappa'+g_{\kappa'},\kappa'}\Lambda_{\kappa+g_\kappa-g_{\kappa'},\kappa+g_\kappa}} \right]. \quad (\text{B3})$$

The calculation in the $n = 4$ case proceeds in a similar manner using the relation $C_4 = \nu_4(m) + 2\nu_2(x)$ and the fact that $2x = -2x(\text{mod } 4)$ to get

$$\Gamma_m^{(4)} = 1 + 2\omega_4^{C_4} \frac{\Lambda_{x,x+g_x}}{\Lambda_{m,m+g_x}} \left[1 - \frac{v(x - m)}{v(g_x)} \frac{\Lambda_{x,m}\Lambda_{m+g_x,x+g_x}}{\Lambda_{m+g_x,m}\Lambda_{x,x+g_x}} \right],$$

$$\Gamma_x^{(4)} = 1 + \frac{1}{2}\omega_4^{-C_4} \frac{\Lambda_{m,m+g_x}}{\Lambda_{x,x+g_x}} \left[1 - \frac{v(x - m)}{v(g_x)} \frac{\Lambda_{m,x}\Lambda_{x+g_x,m+g_x}}{\Lambda_{x+g_x,x}\Lambda_{m,m+g_x}} \right]. \quad (\text{B4})$$

The main difference with the $n = 3$ result is that the Chern number C_4 here appears with opposite signs in the power of ω_4 for $\Gamma_m^{(4)}$ and $\Gamma_x^{(4)}$. Finally, repeating the calculation for $n = 6$ using $C_6 = 2\nu_3(\kappa) - 3\nu_2(m)$ leads to

$$\Gamma_\kappa^{(6)} = 1 + \frac{3}{2}\omega_6^{C_6} \frac{\Lambda_{m,m+g_\kappa}}{\Lambda_{\kappa,\kappa+g_\kappa}} \left[1 - \frac{v(m - \kappa)}{v(g_\kappa)} \frac{\Lambda_{m,\kappa}\Lambda_{\kappa+g_\kappa,m+g_\kappa}}{\Lambda_{\kappa+g_\kappa,\kappa}\Lambda_{m,m+g_\kappa}} \right],$$

$$\Gamma_m^{(6)} = 1 + \frac{2}{3}\omega_6^{-C_6} \frac{\Lambda_{\kappa,\kappa+g_\kappa}}{\Lambda_{m,m+g_\kappa}} \left[1 - \frac{v(m - \kappa)}{v(g_\kappa)} \frac{\Lambda_{\kappa,m}\Lambda_{m+g_\kappa,\kappa+g_\kappa}}{\Lambda_{m+g_\kappa,m}\Lambda_{\kappa,\kappa+g_\kappa}} \right]. \quad (\text{B5})$$

APPENDIX C: EXTENSION TO HOMOBILAYERS

In this appendix, we extend our perturbative calculation of the Chern number to twisted transition metal dichalcogenide (TMD) homobilayers and twisted bilayer graphene (TBG). Because our work discusses only symmetry indicators for the Chern number, we restrict ourselves to the chiral limit of TBG [64], where the topology of the flat bands near charge neutrality is characterized by a sublattice resolved Chern number [60,65]. The main difference between the superlattice case discussed in the main text and the homobilayers discussed here is a doubling of the number of degrees of freedom. In particular, the bare dispersion in the absence of moiré potential now displays two degenerate minima corresponding to the two layers.

1. Twisted transition metal dichalcogenides

Up to a twist-angle-dependent energy scale, the continuum model for the moiré bands of a twisted TMD arising from the K valley of the monolayers takes the form [12,13]

$$H_{\text{TMD}}(v, w, \psi) = H_0(k) + H_m(r), \qquad \text{(C1)}$$

where

$$H_0(k) = (k - \kappa_{\mu_z})^2,$$

$$H_m(r) = 2v \sum_{j=1,3,5} \cos(g_j \cdot r + \mu_z \psi) + w[\mu_+ T(r) + \text{H.c.}],$$

$$T(r) = e^{-i\kappa_+ \cdot r}(e^{-i\kappa_1 \cdot r} + e^{-i\kappa_2 \cdot r} + e^{-i\kappa_3 \cdot r})e^{i\kappa_- \cdot r}, \qquad \text{(C2)}$$

with $\vec{\mu}$ denoting layer Pauli matrices, and where (v, w, ψ) are material-dependent parameters usually extracted from *ab initio* calculations. We also introduce $g_{j=1,\dots,6}$, the moiré reciprocal lattice vector of smallest norm making an angle $(j-1)\pi/3$ with the positive k_x axis, and $\kappa_{j=1,2,3}$, the three equivalent corners of the Brillouin zone making an angle $2(j-1)\pi/3$ with the negative k_y axis, as shown in Fig. 5(a). Our convention is that the minimum of the dispersion relation of the top and bottom layer lie at the $\kappa_+ = \kappa_3$ and the $\kappa_- = -\kappa_2$ points, respectively. The interlayer tunneling $T(r)$ in Eq. (C2) is written to highlight the C_3 symmetry of the model and that $T(r)$ moves one electron from the bottom layer with
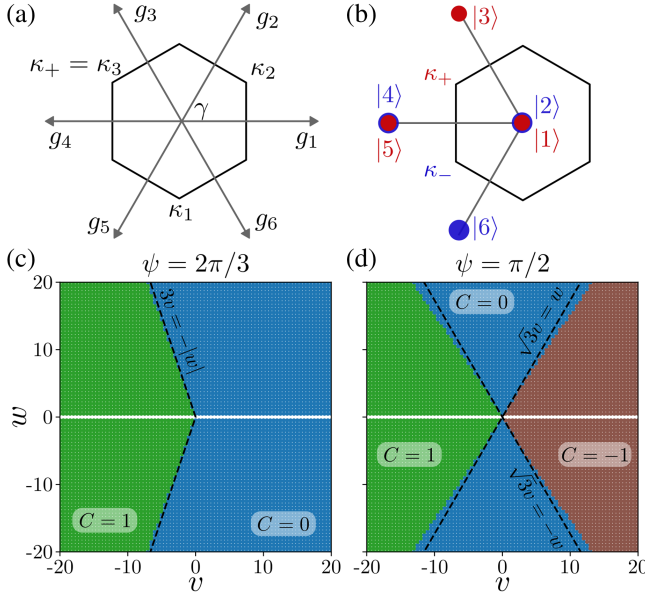

(a) ... g_3 ... g_2 ... $\kappa_+ = \kappa_3$ ... κ_2 ... γ ... g_4 ... g_1 ... g_5 ... κ_1 ... g_6

(b) ... $|3\rangle$ ... κ_+ ... $|4\rangle$ ... $|2\rangle$ ... $|5\rangle$ ... $|1\rangle$ ... κ_- ... $|6\rangle$

(c) $\psi = 2\pi/3$ ... $3v = -|w|$ ... $C = 1$ ... $C = 0$ ... w ... v

(d) $\psi = \pi/2$ ... $C = 0$ ... $\sqrt{3}v = w$ ... $C = 1$ ... $C = -1$ ... $\sqrt{3}v = -w$ ... v

FIG. 5. (a) Moiré BZ indicating the reciprocal lattice vectors $g_{j=1,\dots,6}$ and the zone corners $\kappa_{j=1,2,3}$. (b) The single-particle states $|j = 1, \dots, 6\rangle$, obtained by C_3 rotation of the state at γ in the top (red) and bottom (blue) layers, are degenerate with those at the γ point in the absence of moiré potential ($v = w = 0$). (c),(d) Chern number of the lowest-energy band of the twisted TMD model [Eq. (C1)] for $\psi = 2\pi/3$ (c) and $\psi = \pi/2$ (d) as a function of the material-dependent parameters v and w. Colors show the Chern number obtained by exactly solving the continuum model, while dashed black lines indicate phase boundaries predicted by our perturbative symmetry indicator method. Excellent agreement is found throughout the phase diagram in (c) and for $(v, w) \lesssim 5$ in (d).

dispersion minimum at κ_- to the top layer with the dispersion minimum at κ_+. The moiré bands from the K' valley are obtained by time-reversal conjugation.

Strong Ising spin-orbit coupling in the TMD monolayers induces spin-valley locking at low energy. As a result, spin plays a transparent role in the band topology [66,67], adding only a global minus sign to the formula in Eq. (4), which we discard for the sake of notation consistency. The geometry of the bilayer requires the symmetry indicator with $n = 3$.

As in the main text, we consider the perturbative effect of the moiré Hamiltonian H_m on the bare material dispersion H_0 to determine the C_3 eigenvalues of the lowest-energy band at high-symmetry points of the moiré Brillouin zone. The main difference compared to a superlattice potential applied to a single layer (discussed in the main text) is that the minima of the dispersion for the two layers are located at different positions, i.e., $\kappa_\pm$, which changes the degenerate subspace to consider in the perturbative calculation outlined in Sec. III B.

Specifically, the band minima of the isolated monolayers are also the band minima of the heterobilayer. Thus, the C_3 eigenvalues at the $\kappa_\pm$ points are exactly the C_3 eigenvalues of the bare monolayers at their respective K point. Without loss of generality, this quantity can be taken as unity, i.e., $\nu_3(\kappa_\pm) = 0$, as the orbital content of the monolayers contributes an overall phase $e^{2i\pi/3}$ to the representation of C_3 for all high-symmetry points, which cancels in the symmetry indicator formula Eq. (4) [68].

To determine the Chern number of the lowest moiré band of Eq. (C1), it remains to determine the C_3 eigenvalue of the perturbative ground state at the γ point. This ground state has already been obtained in Appendix D in Ref. [13]; we now review its construction. Let $|j = 1, 3, 5\rangle$ denote the plane wave in the top layer with momentum $k_j = \kappa_+ + (g_j + g_{j-1})/3$ and $|j = 2, 4, 6\rangle$ the plane wave in the bottom layer with momentum $k_j = \kappa_- + (g_j + g_{j-1})/3$. As can be seen in Fig. 5(b), these states transform as $C_3|j\rangle = |j + 2\rangle$ under $2\pi/3$ rotations centered at the minimum of the top (j odd) and bottom (j even) moiré BZ—making them degenerate in energy in the absence of moiré potentials ($v = w = 0$). As in the main text, the discrete Fourier transformation

$$|n\rangle = \frac{1}{\sqrt{6}} \sum_{j=1}^{6} e^{2inj\pi/3}|j\rangle \qquad \text{(C3)}$$

perturbatively diagonalizes the moiré Hamiltonian H_m, yielding the eigenenergies

$$\varepsilon_n^{\text{TMD}}(v, w, \psi) = 2w\cos(\pi n/3) + 2v\cos(\psi - 2n\pi/3) \qquad \text{(C4)}$$

for the state $|n\rangle$ with C_3 eigenvalue $e^{2in\pi/3}$. Combined with $\nu_3(\kappa_\pm) = 0$, the symmetry indicator formula Eq. (4)

dictates that the lowest moiré band is topologically trivial if the minimum ε_n is given by $n \in \{0, 3\}$; has Chern number 1 modulo 3 if $n \in \{1, 4\}$; and has Chern number -1 modulo 3 if $n \in \{2, 5\}$.

To demonstrate the predictive power of this method, let us take $\psi = 2\pi/3$ [14] and compare the Chern number obtained from the perturbative symmetry indicator result to that obtained by solving the full continuum model in Eq. (C1). For this choice of angle ψ, Eq. (C4) gives a Chern number equal to 1 when $3v < -|w|$ and equal to zero otherwise. This perfectly matches the results of the full continuum model, as shown in Fig. 5(c). This agreement demonstrates the accuracy of our perturbative symmetry indicator method for the twisted TMD bilayers. In Fig. 5(d), we show the results for $\psi = \pi/2$, for which Eq. (C4) predicts a Chern number equal to 0 when $|w| > \sqrt{3}|v|$ and away from this region gives a Chern number 1 when $\sqrt{3}v < -|w|$ and to -1 when $\sqrt{3}v > |w|$. Again, the results of the full continuum model and of our perturbative expansion agree very well for small values of v and w; they deviate slightly as these two coefficients become very large, corresponding to the small twist angle limit.

2. Chiral twisted bilayer graphene

To apply our results to TBG, we consider the chiral limit, where the same-orbital interlayer hopping is discarded [64], resulting in a purely off-diagonal Hamiltonian in the sublattice degree of freedom and sublattice-polarized flat bands at the magic angle [60,65]. One way to compute the Chern number of these bands is to square the chiral TBG Hamiltonian, which, owing to the off-diagonal structure of the Hamiltonian, decouples the A and B sublattices as

$$H_{\text{TBG}}^2(\alpha) = \begin{bmatrix} H_A(\alpha) & 0 \\ 0 & H_B(\alpha) \end{bmatrix}. \quad (C5)$$

The resulting squared Hamiltonian depends on only α, the ratio of interlayer tunneling to Fermi velocity. The functional form of $H_{A/B}$ takes the form [14]

$$H_A(\alpha) = H_{\text{TMD}}(|\alpha|^2, \alpha, \psi = 2\pi/3) + [\tilde{T}_k(r)\mu_+ + \text{H.c.}],$$

$$\tilde{T}_k(r) = \frac{2i\alpha}{|\kappa_+|^2} e^{-i\kappa_+ \cdot r} \left(\sum_{j=1,2,3} e^{-i\kappa_j \cdot r} \kappa_j \times k \right) e^{i\kappa_- \cdot r}. \quad (C6)$$

The Chern number of the band from H_B is opposite to that from H_A [60], and we consider only $H_A(\alpha)$ from now on. Projecting this Hamiltonian in the perturbative basis defined in Eq. (C3), we find an additional term in the energy

$$\varepsilon_n^{\text{TBG}} = \varepsilon_n^{\text{TMD}}(|\alpha|^2, \alpha, 2\pi/3) - 2\sqrt{3}\alpha \sin(\pi n/3)$$

$$= 2|\alpha|^2 \cos[2(n-1)\pi/3] + 4\alpha \cos[\pi(n+1)/3]. \quad (C7)$$

This energy is minimized by $n = 2$ when $\alpha > 0$ and $n = 5$ when $\alpha < 0$, both resulting in a C_3 eigenvalue of $\nu_3^A(\gamma) = -1$. Reproducing the equation for the other sublattice $H_B(\alpha)$ yields an opposite value $\nu_3^B(\gamma) = 1$, as required by the symmetry of the model [60]. In summary, for all α, our perturbative calculation predicts a sublattice-polarized Chern number of ± 1, opposite for the two sublattices. Remarkably, this matches the result of the Bistritzer-MacDonald model in the chiral limit [60,64]. The agreement comes because our perturbative method is justified at small α and the Chern number in the chiral limit remains the same for any value of α.

———————

[1] E. Y. Andrei, D. K. Efetov, P. Jarillo-Herrero, A. H. MacDonald, K. F. Mak, T. Senthil, E. Tutuc, A. Yazdani, and A. F. Young, *The marvels of moiré materials*, Nat. Rev. Mater. **6,** 201 (2021).

[2] K. F. Mak and J. Shan, *Semiconductor moiré materials*, Nat. Nanotechnol. **17,** 686 (2022).

[3] S. A. A. Ghorashi, A. Dunbrack, A. Abouelkomsan, J. Sun, X. Du, and J. Cano, *Topological and stacked flat bands in bilayer graphene with a superlattice potential*, Phys. Rev. Lett. **130,** 196201 (2023).

[4] K. P. Nuckolls and A. Yazdani, *A microscopic perspective on moiré materials*, Nat. Rev. Mater. **9,** 460 (2024).

[5] K. Uchida, S. Furuya, J.-I. Iwata, and A. Oshiyama, *Atomic corrugation and electron localization due to moiré patterns in twisted bilayer graphenes*, Phys. Rev. B **90,** 155451 (2014).

[6] J. Jung, A. Raoux, Z. Qiao, and A. H. MacDonald, *Ab initio theory of moiré superlattice bands in layered two-dimensional materials*, Phys. Rev. B **89,** 205414 (2014).

[7] S. Carr, D. Massatt, S. Fang, P. Cazeaux, M. Luskin, and E. Kaxiras, *Twistronics: Manipulating the electronic properties of two-dimensional layered structures through their twist angle*, Phys. Rev. B **95,** 075420 (2017).

[8] D. Massatt, M. Luskin, and C. Ortner, *Electronic density of states for incommensurate layers*, Multiscale Model. Simul. **15,** 476 (2017).

[9] Y. Zhang, T. Liu, and L. Fu, *Electronic structures, charge transfer, and charge order in twisted transition metal dichalcogenide bilayers*, Phys. Rev. B **103,** 155142 (2021).

[10] T. Zhang, N. Regnault, B. A. Bernevig, X. Dai, and H. Weng, *O(n) ab initio calculation scheme for large-scale moiré structures*, Phys. Rev. B **105,** 125127 (2022).

[11] R. Bistritzer and A. H. MacDonald, *Moiré bands in twisted double-layer graphene*, Proc. Natl. Acad. Sci. U.S.A. **108,** 12233 (2011).

[12] F. Wu, T. Lovorn, E. Tutuc, I. Martin, and A. H. MacDonald, *Topological insulators in twisted transition metal dichalcogenide homobilayers*, Phys. Rev. Lett. **122,** 086402 (2019).

[13] T. Devakul, V. Crépel, Y. Zhang, and L. Fu, *Magic in twisted transition metal dichalcogenide bilayers*, Nat. Commun. **12,** 6730 (2021).

[14] V. Crépel, N. Regnault, and R. Queiroz, *Chiral limit and origin of topological flat bands in twisted transition metal*

dichalcogenide homobilayers, Commun. Phys. **7**, 146 (2024).

[15] O. Vafek and J. Kang, *Continuum effective Hamiltonian for graphene bilayers for an arbitrary smooth lattice deformation from microscopic theories*, Phys. Rev. B **107**, 075123 (2023).

[16] T. Kong, D. Liu, M. Luskin, and A. B. Watson, *Modeling of electronic dynamics in twisted bilayer graphene*, SIAM J. Appl. Math. **84**, 1011 (2024).

[17] C. Fang, M. J. Gilbert, and B. A. Bernevig, *Bulk topological invariants in noninteracting point group symmetric insulators*, Phys. Rev. B **86**, 115112 (2012).

[18] C. Forsythe, X. Zhou, K. Watanabe, T. Taniguchi, A. Pasupathy, P. Moon, M. Koshino, P. Kim, and C. R. Dean, *Band structure engineering of 2d materials using patterned dielectric superlattices*, Nat. Nanotechnol. **13**, 566 (2018).

[19] B. S. Jessen, L. Gammelgaard, M. R. Thomsen, D. M. A. Mackenzie, J. D. Thomsen, J. Caridad, E. Duegaard, K. Watanabe, T. Taniguchi, T. J. Booth, T. G. Pedersen, A.-P. Jauho, and P. Bøggild, *Lithographic band structure engineering of graphene*, Nat. Nanotechnol. **14**, 340 (2019).

[20] Y. Li, S. Dietrich, C. Forsythe, T. Taniguchi, K. Watanabe, P. Moon, and C. R. Dean, *Anisotropic band flattening in graphene with one-dimensional superlattices*, Nat. Nanotechnol. **16**, 525 (2021).

[21] J. Cano, S. Fang, J. H. Pixley, and J. H. Wilson, *Moiré superlattice on the surface of a topological insulator*, Phys. Rev. B **103**, 155157 (2021).

[22] T. Wang, N. F. Q. Yuan, and L. Fu, *Moiré surface states and enhanced superconductivity in topological insulators*, Phys. Rev. X **11**, 021024 (2021).

[23] D. Barcons Ruiz, H. Herzig Sheinfux, R. Hoffmann, I. Torre, H. Agarwal, R. K. Kumar, L. Vistoli, T. Taniguchi, K. Watanabe, A. Bachtold, and F. H. L. Koppens, *Engineering high quality graphene superlattices via ion milled ultra-thin etching masks*, Nat. Commun. **13**, 6926 (2022).

[24] D. Guerci, J. Wang, J. H. Pixley, and J. Cano, *Designer meron lattice on the surface of a topological insulator*, Phys. Rev. B **106**, 245417 (2022).

[25] J. Sun, S. A. Akbar Ghorashi, K. Watanabe, T. Taniguchi, F. Camino, J. Cano, and X. Du, *Signature of correlated insulator in electric field controlled superlattice*, Nano Lett. **24**, 13600 (2024).

[26] S. A. A. Ghorashi and J. Cano, *Multilayer graphene with a superlattice potential*, Phys. Rev. B **107**, 195423 (2023).

[27] A. De Martino, L. Dell'Anna, L. Handt, A. Miserocchi, and R. Egger, *Two-dimensional Dirac fermions in a mass superlattice*, Phys. Rev. B **107**, 115420 (2023).

[28] Y. Zeng, T. M. R. Wolf, C. Huang, N. Wei, S. A. A. Ghorashi, A. H. MacDonald, and J. Cano, *Gate-tunable topological phases in superlattice modulated bilayer graphene*, Phys. Rev. B **109**, 195406 (2024).

[29] J. C. Song, P. Samutpraphoot, and L. S. Levitov, *Topological Bloch bands in graphene superlattices*, Proc. Natl. Acad. Sci. U.S.A. **112**, 10879 (2015).

[30] E. M. Spanton, A. A. Zibrov, H. Zhou, T. Taniguchi, K. Watanabe, M. P. Zaletel, and A. F. Young, *Observation of fractional Chern insulators in a van der Waals heterostructure*, Science **360**, 62 (2018).

[31] F. Wu, T. Lovorn, E. Tutuc, and A. H. MacDonald, *Hubbard model physics in transition metal dichalcogenide moiré bands*, Phys. Rev. Lett. **121**, 026402 (2018).

[32] Y.-H. Zhang, D. Mao, Y. Cao, P. Jarillo-Herrero, and T. Senthil, *Nearly flat Chern bands in moiré superlattices*, Phys. Rev. B **99**, 075127 (2019).

[33] B. L. Chittari, G. Chen, Y. Zhang, F. Wang, and J. Jung, *Gate-tunable topological flat bands in trilayer graphene boron-nitride moiré superlattices*, Phys. Rev. Lett. **122**, 016401 (2019).

[34] G. Chen, A. L. Sharpe, E. J. Fox, Y.-H. Zhang, S. Wang, L. Jiang, B. Lyu, H. Li, K. Watanabe, T. Taniguchi *et al.*, *Tunable correlated Chern insulator and ferromagnetism in a moiré superlattice*, Nature (London) **579**, 56 (2020).

[35] V. Crépel, A. Dunbrack, D. Guerci, J. Bonini, and J. Cano, *Chiral model of twisted bilayer graphene realized in a monolayer*, Phys. Rev. B **108**, 075126 (2023).

[36] Z. Lu, T. Han, Y. Yao, A. P. Reddy, J. Yang, J. Seo, K. Watanabe, T. Taniguchi, L. Fu, and L. Ju, *Fractional quantum anomalous Hall effect in multilayer graphene*, Nature (London) **626**, 759 (2024).

[37] K. Yang, Z. Xu, Y. Feng, F. Schindler, Y. Xu, Z. Bi, B. A. Bernevig, P. Tang, and C.-X. Liu, *Topological minibands and interaction driven quantum anomalous Hall state in topological insulator based moiré heterostructures*, Nat. Commun. **15**, 2670 (2024).

[38] J. Xie, Z. Huo, X. Lu, Z. Feng, Z. Zhang, W. Wang, Q. Yang, K. Watanabe, T. Taniguchi, K. Liu *et al.*, *Even-and odd-denominator fractional quantum anomalous Hall effect in graphene moire superlattices*, arXiv:2405.16944.

[39] J. Dong, T. Wang, T. Wang, T. Soejima, M. P. Zaletel, A. Vishwanath, and D. E. Parker, *Anomalous Hall crystals in rhombohedral multilayer graphene. I. Interaction-driven Chern bands and fractional quantum Hall states at zero magnetic field*, Phys. Rev. Lett. **133**, 206503 (2024).

[40] Z. Dong, A. S. Patri, and T. Senthil, *Theory of quantum anomalous Hall phases in pentalayer rhombohedral graphene moiré structures*, Phys. Rev. Lett. **133**, 206502 (2024).

[41] B. Zhou, H. Yang, and Y.-H. Zhang, *Fractional quantum anomalous Hall effect in rhombohedral multilayer graphene in the moiréless limit*, Phys. Rev. Lett. **133**, 206504 (2024).

[42] Z. Guo, X. Lu, B. Xie, and J. Liu, *Fractional Chern insulator states in multilayer graphene moiré superlattices*, Phys. Rev. B **110**, 075109 (2024).

[43] X.-Y. Song, C.-M. Jian, L. Fu, and C. Xu, *Intertwined fractional quantum anomalous Hall states and charge density waves*, Phys. Rev. B **109**, 115116 (2024).

[44] Y. Zeng, D. Guerci, V. Crépel, A. J. Millis, and J. Cano, *Sublattice structure and topology in spontaneously crystallized electronic states*, Phys. Rev. Lett. **132**, 236601 (2024).

[45] Z. Dong, A. S. Patri, and T. Senthil, *Stability of anomalous Hall crystals in multilayer rhombohedral graphene*, Phys. Rev. B **110**, 205130 (2024).

[46] J. Herzog-Arbeitman, Y. Wang, J. Liu, P. M. Tam, Z. Qi, Y. Jia, D. K. Efetov, O. Vafek, N. Regnault, H. Weng *et al.*, *Moiré fractional Chern insulators. II. First-principles calculations and continuum models of rhombohedral graphene superlattices*, Phys. Rev. B **109**, 205122 (2024).

[47] Y. Su, H. Li, C. Zhang, K. Sun, and S.-Z. Lin, *Massive Dirac fermions in moiré superlattices: A route towards topological flat minibands and correlated topological insulators*, Phys. Rev. Res. **4**, L032024 (2022).

[48] N. Suri, C. Wang, B. M. Hunt, and D. Xiao, *Superlattice engineering of topology in massive Dirac fermions*, Phys. Rev. B **108**, 155409 (2023).

[49] T. Soejima, J. Dong, T. Wang, T. Wang, M. P. Zaletel, A. Vishwanath, and D. E. Parker, *Anomalous Hall crystals in rhombohedral multilayer graphene. II. General mechanism and a minimal model*, Phys. Rev. B **110**, 205124 (2024).

[50] S. Sarkar, X. Wan, S.-Z. Lin, and K. Sun, *Symmetry-based classification of exact flat bands in single and bilayer moiré systems*, arXiv:2310.02218.

[51] M. G. Scheer and B. Lian, *Kagome and honeycomb flat bands in moiré graphene*, Phys. Rev. B **108**, 245136 (2023).

[52] T. Tan, A. P. Reddy, L. Fu, and T. Devakul, *Designing topology and fractionalization in narrow gap semiconductor films via electrostatic engineering*, Phys. Rev. Lett. **133**, 206601 (2024).

[53] F. Zhang, B. Sahu, H. Min, and A. H. MacDonald, *Band structure of ABC-stacked graphene trilayers*, Phys. Rev. B **82**, 035409 (2010).

[54] M. Koshino, *Interlayer screening effect in graphene multilayers with ABA and ABC stacking*, Phys. Rev. B **81**, 125304 (2010).

[55] H. Zhou, T. Xie, A. Ghazaryan, T. Holder, J. R. Ehrets, E. M. Spanton, T. Taniguchi, K. Watanabe, E. Berg, M. Serbyn *et al.*, *Half-and quarter-metals in rhombohedral trilayer graphene*, Nature (London) **598**, 429 (2021).

[56] Y. H. Kwan, J. Yu, J. Herzog-Arbeitman, D. K. Efetov, N. Regnault, and B. A. Bernevig, *Moiré fractional Chern insulators III: Hartree-Fock phase diagram, magic angle regime for Chern insulator states, the role of the moiré potential and Goldstone gaps in rhombohedral graphene superlattices*, arXiv:2312.11617.

[57] P. Moon and M. Koshino, *Electronic properties of graphene/hexagonal-boron-nitride moiré superlattice*, Phys. Rev. B **90**, 155406 (2014).

[58] Y. Park, Y. Kim, B. L. Chittari, and J. Jung, *Topological flat bands in rhombohedral tetralayer and multilayer graphene on hexagonal boron nitride moire superlattices*, Phys. Rev. B **108**, 155406 (2023).

[59] H. Min and A. H. MacDonald, *Chiral decomposition in the electronic structure of graphene multilayers*, Phys. Rev. B **77**, 155416 (2008).

[60] Z.-D. Song, B. Lian, N. Regnault, and B. A. Bernevig, *Twisted bilayer graphene. II. Stable symmetry anomaly*, Phys. Rev. B **103**, 205412 (2021).

[61] H. C. Po, *Symmetry indicators of band topology*, J. Phys. Condens. Matter **32**, 263001 (2020).

[62] B. Bradlyn, L. Elcoro, J. Cano, M. G. Vergniory, Z. Wang, C. Felser, M. I. Aroyo, and B. A. Bernevig, *Topological quantum chemistry*, Nature (London) **547**, 298 (2017).

[63] L. Elcoro, B. J. Wieder, Z. Song, Y. Xu, B. Bradlyn, and B. A. Bernevig, *Magnetic topological quantum chemistry*, Nat. Commun. **12**, 5965 (2021).

[64] G. Tarnopolsky, A. J. Kruchkov, and A. Vishwanath, *Origin of magic angles in twisted bilayer graphene*, Phys. Rev. Lett. **122**, 106405 (2019).

[65] V. Crépel, P. Ding, N. Verma, N. Regnault, and R. Queiroz, *Topologically protected flatness in chiral moiré heterostructures*, arXiv:2403.19656.

[66] Y. Zhang, T. Devakul, and L. Fu, *Spin-textured Chern bands in AB-stacked transition metal dichalcogenide bilayers*, Proc. Natl. Acad. Sci. U.S.A. **118**, e2112673118 (2021).

[67] V. Crépel and A. Millis, *Bridging the small and large in twisted transition metal dichalcogenide homobilayers: A tight binding model capturing orbital interference and topology across a wide range of twist angles*, Phys. Rev. Res. **6**, 033127 (2024).

[68] Y. Jia, J. Yu, J. Liu, J. Herzog-Arbeitman, Z. Qi, H. Pi, N. Regnault, H. Weng, B. A. Bernevig, and Q. Wu, *Moiré fractional Chern insulators. I. First-principles calculations and continuum models of twisted bilayer mote 2*, Phys. Rev. B **109**, 205121 (2024).